Inorganic Chemistry

pubs.acs.org/IC Forum Article

Cation Distribution in Spinel Ferrite Nanocrystals: Characterization, Impact on their Physical Properties, and Opportunities for Synthetic Control

Karla R. Sanchez-Lievanos, James L. Stair, and Kathryn E. Knowles*



Cite This: Inorg. Chem. 2021, 60, 4291-4305

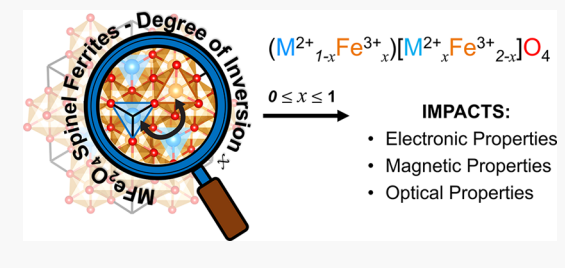


ACCESS I

III Metrics & More

Article Recommendations

ABSTRACT: Metal oxide materials that adopt the spinel crystal structure, such as metal ferrites (MFe₂O₄), present tetrahedral (A) and octahedral [B] sublattice sites surrounded by oxygen anions that provide a relatively weak crystal-field splitting. The formula of a metal ferrite material is most precisely described as $(M_{1-x}Fe_x)[M_xFe_{2-x}]O_4$, where the parentheses and square brackets denote the tetrahedral and octahedral sites, respectively, and x is the inversion parameter quantifying the distribution of M^{2+} and Fe^{3+} cations among these sites. The electronic, magnetic, and optical properties of spinel ferrites all depend on the magnitude of x, which, in turn, depends on the



relative sizes of the cations, their charge, and the relative crystal-field stabilization afforded by tetrahedral or octahedral coordination. Compared to bulk spinel ferrites, the large surface-area-to-volume ratio of spinel ferrite nanocrystals provides additional structural degrees of freedom that enable access to a broader range of x values. Achieving synthetic control over the degree of inversion in addition to the size and shape is critical to tuning the properties of spinel ferrite nanocrystals. In this Forum Article, we review physical inorganic methods used to quantify x in spinel ferrite nanocrystals, describe how the electronic, magnetic, and optical properties of these nanocrystals depend on x, and discuss emerging strategies for achieving synthetic control over this parameter.

■ INTRODUCTION

Ternary metal oxides comprise a diverse set of compositions and crystal structures and are thus one of the largest and most multifunctional classes of solid materials. 1-3 These materials offer significant flexibility in tailoring optical, magnetic, and electronic properties by virtue of the close interaction between two different metal cations within the crystal lattice sites, which enables synergistic effects not manifested in binary oxide phases.^{4,5} In particular, nanostructured and bulk spinel ferrites of the formula MFe₂O₄, where M is a divalent metal cation, exhibit high resistance to wear and corrosion, high saturation magnetization, and narrow band gaps (~2 eV). 6-8 Additionally, these materials are composed of elements with a high natural abundance, and their consequently low production costs make them attractive for a wide range of applications in various fields of science and technology, such as photocatalysis, storage and transformation of energy, magnetic drug delivery, and gas sensors. 9-18

Spinel ferrites are mixed-valent, mixed-metal oxides that crystallize in the spinel phase, which belongs to the cubic $Fd\overline{3}m$ space group with a unit cell containing eight formula units, $M_8Fe_{16}O_{32}$ (Figure 1). Within this structure, the oxygen anions form a cubic close-packed lattice, and the metal cations occupy one-eighth of the tetrahedral (A) and half of the octahedral [B] interstitial sites of the lattice. This family of materials has the general formula $(M^{2+}_{1-x}Fe^{3+}_{x})[M^{2+}_{x}Fe^{3+}_{2-x}]O_{4y}$ where x is the

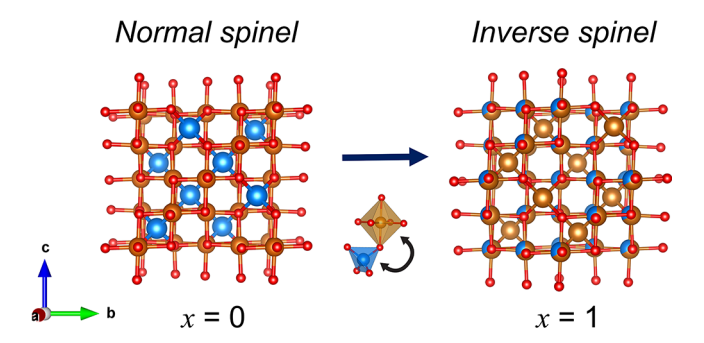


Figure 1. Unit cells of representative normal (left) and inverse (right) spinel ferrites. The oxygen positions are marked in red; the orange and blue spheres represent the Fe³⁺ and M²⁺ ions, respectively. The exchange of metal ions between the (A) and [B] sites impacts the electronic, optical, and magnetic properties of the material.

Special Issue: Inorganic Chemistry of Nanoparticles

Received: January 6, 2021 Published: March 18, 2021





inversion parameter that quantifies the distribution of the divalent cation M^{2+} and the trivalent cation Fe^{3+} across the (A) and [B] sites. There are four main subcategories of spinel ferrites defined by the value of x: (i) x=0 yields a normal spinel, (ii) x=1 yields an inverse spinel, (iii) $x=\frac{2}{3}$ indicates a fully randomized spinel, and (iv) 0 < x < 1 yields a mixed or partially inverted spinel. The relative preference of the two metal cations to occupy octahedral or tetrahedral sites depends on the ionic radius, size of the interstitial site, ionic charge, and crystal-field stabilization energy. $^{16-19}$

The magnitude of the inversion parameter in spinel ferrite nanocrystals can be significantly different from that found in bulk samples of the same composition. The increased structural degrees of freedom imparted to nanocrystals by virtue of their large surface-area-to-volume ratios enables access to a broader range of inversion parameters in nanostructured spinel ferrites than are available to the corresponding bulk materials. The magnitude of the deviation of the inversion parameter from the bulk value depends on the synthetic method and, for some compositions and synthetic methods, may correlate with the size of the nanocrystals. For example, $ZnFe_2O_4$, which adopts a normal configuration (x=0) in the bulk, generally tends to become increasingly inverted as the nanocrystal size decreases (Figure 2), although some

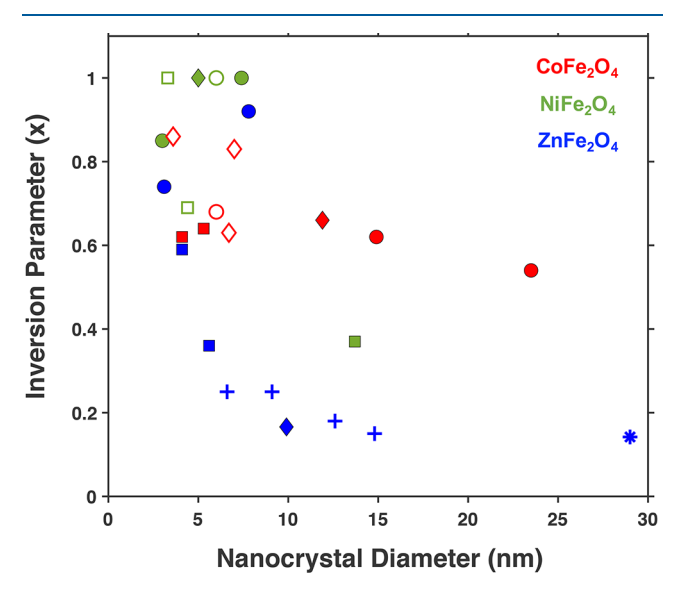


Figure 2. Plot of the inversion parameter versus nanocrystal diameter for $CoFe_2O_4$ (red), $NiFe_2O_4$ (green), and $ZnFe_2O_4$ (blue) nanocrystals. Data are taken from refs 18 (crosses), 20 (solid circles), 21 (open circles), 22 (solid diamonds), 23 (solid squares), 24 (open diamonds), 25 (open squares), and 26 (asterisk).

synthetic methods may produce the opposite trend.²⁰ For a given synthesis, any correlation between the size and inversion parameter could be due to a mutual dependence of both properties on the same synthetic parameter (e.g., ligand concentration or temperature) rather than a direct causal relationship. In contrast, NiFe₂O₄ and CoFe₂O₄ nanocrystals exhibit a much weaker to no correlation between the nanocrystal size and degree of inversion (Figure 2). Because the electronic, magnetic, and optical properties of spinel ferrites are governed in part by the degree of inversion, nanocrystalline spinel ferrites provide the opportunity to tune these properties over a much broader range than is possible for the bulk materials.

In this Forum Article, we discuss the impact of the degree of inversion of a series of ternary spinel ferrite nanocrystals with the formula MFe_2O_4 , where $M=Mg^{2+}$, Mn^{2+} , Co^{2+} , Ni^{2+} , Cu^{2+} , or Zn^{2+} , on their physicochemical properties. We also discuss methods used to quantify the degree of inversion and emerging strategies to achieve synthetic control over this parameter.

METHODS TO MEASURE THE DEGREE OF INVERSION

This section describes physical inorganic methods used to quantify the site occupancies of cations, i.e., degree of inversion, within spinel ferrite nanocrystals. Many of these methods rely on the sensitivity of spectroscopic transitions involving core electrons of the metal cations (in the case of the X-ray spectroscopies and electron energy loss spectroscopy, EELS) or nuclear transitions of the iron centers (in the case of Mössbauer spectroscopy) to changes in the metal's local coordination sphere. Other methods, such as neutron diffraction and Raman spectroscopy, are sensitive to the long-range ordering or symmetry of the nanocrystals, which is influenced by the degree of inversion. Here we describe briefly how each technique can be used to quantify x.

Mössbauer Spectroscopy. Mössbauer spectroscopy is a particularly valuable technique that gives precise information about the chemical, structural, and magnetic properties of a material that contains an isotope with a strong nuclear quadrupole moment, such as ⁵⁷Fe. It is based on the Doppler effect and the recoil-less γ -ray emission and absorption, known as the Mössbauer effect. Mössbauer spectra are defined by three parameters. 27 (i) The isomer shift (δ) arises from the difference in the s-electron density between the source and absorber and indicates the valence state of iron. Because the loss of an electron in the d orbital (e.g., from Fe^{2+} to Fe^{3+} or from Fe^{3+} to Fe⁴⁺) causes a higher relative s-electron density at the ⁵⁷Fe nucleus, higher oxidation states of iron lead to smaller isomer shifts. ²⁸ (ii) The nuclear electric quadrupole splitting ($\Delta E_{\rm O}$) arises from a shift in the nuclear energy levels induced by an anisotropic electric-field gradient caused by nearby electrons. The magnitude of $\Delta E_{\rm Q}$ reflects the coordination environment of the iron atoms. (iii) The nuclear magnetic hyperfine splitting (B_{hf}) is sensitive to the spin state of the iron and magnetic ordering within the sample. This technique provides a particularly valuable analytical tool for iron-based materials because the shape of the Mössbauer spectrum is affected by the oxidation state of iron, its electronic configuration, the symmetry of its crystallographic site, the presence/absence of magnetic ordering (temperature-dependent), and the ligand field surrounding the iron nuclei.29

In addition to being exquisitely sensitive to the electronic structure and bonding around iron nuclei, Mössbauer spectroscopy is particularly useful for characterizing magnetic nanoparticles because the time scale of the measurement is on the order of the time scale of magnetic relaxation observed in superparamagnetic particles given by the Néel-Brown expression (eq 1):

$$\tau = \tau_0 \exp(KV/k_{\rm B}T) \tag{1}$$

where τ_0 (the reciprocal of the natural frequency of the gyromagnetic precession) is typically in the range $10^{-9}-10^{-12}$ s, K is the magnetic anisotropic energy constant, V is the volume of the particle, $k_{\rm B}$ is the Boltzmann constant, and T is the temperature. The is shorter than the time scale of the measurement, the average value of the internal magnetic field at individual iron sites is zero. Under these conditions, the Mössbauer spectrum has a doublet line shape arising from quadrupolar splitting of the I=3/2 excited nuclear state into $m_I=\pm^1/2$ and $\pm^3/2$ (Figure 3). In contrast, when τ is on the order of or longer than the time scale of the measurement, the individual iron nuclei experience a nonzero magnetic field that induces a Zeeman splitting of the nuclear spin states and leads to six allowed transitions with $\Delta m_I=\pm 1$ or 0 (Figure 3). The spectrum therefore exhibits a sextet splitting pattern under these conditions. Because τ increases with decreasing temperature according to eq 1, the Mössbauer spectra of

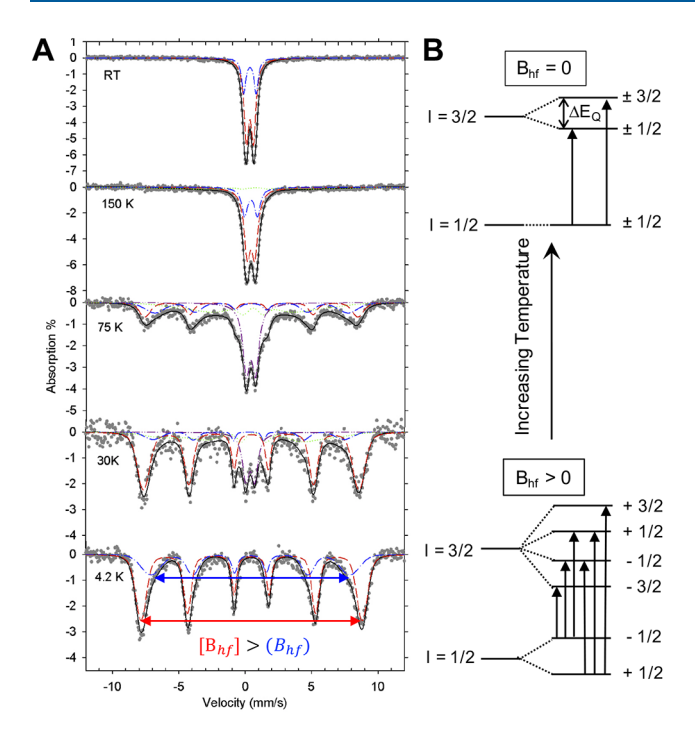


Figure 3. (A) Mössbauer spectra associated with 2.6-nm-diameter nanoparticles of $CoFe_2O_4$ at various temperatures. The solid lines through the experimental points represent least-squares fits of the data to a superposition of quadrupolar and magnetic spectra associated with iron occupying tetrahedral (blue) and octahedral (red) sites. At intermediate temperatures, a dynamic, intermediate relaxation envelope (green) was also included. Adapted with permission from ref 20. Copyright 2015 American Chemical Society. (B) Energy-level diagrams depicting the allowed nuclear transitions in the absence (top) and presence (bottom) of hyperfine splitting induced by a net internal magnetic field B_{hf} .

many magnetic nanoparticles evolve from a doublet splitting pattern into a sextet splitting pattern as the temperature decreases (Figure 3). 31,32

For spinel ferrites, the internal magnetic field experienced by iron nuclei occupying octahedral [B] sites is larger than that experienced by iron nuclei occupying tetrahedral (A) sites due to the dipolar field originating from the deviation from cubic symmetry in the tetrahedral site and the stronger orbital overlap between the iron sites in the smaller tetrahedral site and the surrounding oxygen anions. This difference produces two overlapping sextet patterns at low temperature whose areas are proportional to the numbers of iron nuclei occupying the (A) and (B) sites. Thus, the relative areas of these two sextet peaks can be used to quantify the inversion parameter x according to eq 2 (assuming that the recoil-free fractions of the (A) and (B) sites are equal).

$$x = 2 \frac{(Fe^{3+})_{area}}{(Fe^{3+})_{area} + [Fe^{3+}]_{area}}$$
(2)

For example, Figure 3 plots temperature-dependent Mössbauer spectra collected for $CoFe_2O_4$ nanocrystals with a diameter of 2.6 nm. ²⁰ At room temperature, the spectrum contains a doublet peak corresponding to a quadrupolar splitting in the absence of a net internal magnetic field and indicates rapid magnetic relaxation. As the temperature decreases, the doublet converts into a sextet splitting pattern. At 4 K, the spectrum comprises two overlapping sextets: one corresponds to a hyperfine field of 51.5 ± 0.5 T and accounts for $66 \pm 5\%$ of the spectral intensity, and the other corresponds to a hyperfine field of 46.4 ± 0.5 T and accounts for $34 \pm 5\%$ of the spectral intensity. The sextet peak with the smaller hyperfine field was assigned

to the tetrahedral iron sites, and the inversion parameter calculated from these data using eq 2 is x = 0.68.

Neutron Diffraction. The lattice parameter of a spinel ferrite depends in part on the magnitude of the inversion parameter due to the differences in the ionic radii of the M²⁺ and Fe³⁺ ions. As the degree of inversion increases, more of the smaller tetrahedral sites are occupied by Fe3+ cations and M2+ ions occupy more of the larger octahedral sites. Because the radius of Fe³⁺ is smaller than that of M²⁺ when M is Mg or a late-first-row transition metal, shifting Fe³⁺ cations into smaller tetrahedral sites causes the size of the unit cell to contract, thereby decreasing the lattice parameter. 19,37,38 However, the degree of inversion in spinel ferrite nanocrystals cannot be quantified precisely based on the lattice parameter alone because other factors, such as lattice strain, also impact the lattice parameter on the nanoscale. In fact, the cation site distribution in transitionmetal spinel ferrites is difficult to quantify precisely using powder Xray diffraction because the electron density surrounding the Fe3+ centers is too similar to that surrounding the M2+ centers, rendering them indistinguishable. In contrast, neutrons scatter and diffract off of the nuclei of atoms rather than their electron density. ³⁹ Consequently, the neutron scattering length for iron is very different from that of other 3d metals. Therefore, Rietveld refinement of neutron powder diffraction data can be used to quantify precisely the inversion parameter of spinel ferrites. ^{23,40} Rietveld refinement involves fitting of the shapes and intensities of the diffraction peaks in order to determine the crystallite size, site occupancies, atomic displacement parameters, and ratios of various crystal phases and compositions that may be present in a mixture, in addition to the lattice parameter and crystal structure identification determined by the positions of the peaks. Additionally, because neutrons have spin, their scattering interactions with nuclei are impacted by the spin of the surrounding electrons. Neutron powder diffraction spectra are therefore also sensitive to magnetic ordering within a sample.³

Figure 4 shows neutron powder diffraction patterns collected for $CoFe_2O_4$ and $ZnFe_2O_4$ nanocrystals. The spectra calculated from the Rietveld refinement procedure indicate inversion parameters of x=0.66 for $CoFe_2O_4$ and 0.166 for $ZnFe_2O_4$. The solid red lines indicate the contribution of magnetic ordering to the overall diffraction pattern. These data indicate that $CoFe_2O_4$ exhibits significant magnetic ordering that contributes to several diffraction peaks, whereas $ZnFe_2O_4$ exhibits very little magnetic order. In particular, magnetic ordering in $CoFe_2O_4$ contributes significant intensity to the diffraction peaks at $q \sim 1.3$, 2.6, and 3.25 Å $^{-1}$, whereas the latter two peaks are absent from the $ZnFe_2O_4$ spectrum.

Raman Spectroscopy. Normal spinel ferrites crystallize in the cubic space group $Fd\overline{3}m$. Factor group analysis predicts five first-order Raman-active phonon modes for this space group: one A_{1g} mode, one E_g mode, and three T_{2g} modes. $^{41-43}$ The A_{1g} mode is associated with symmetric stretching of the M–O bonds at the tetrahedral site along the $\langle 111 \rangle$ direction, 44 the E_g mode is associated with symmetric bending of the M–O bonds at the octahedral site, and the T_{2g} modes are due to asymmetric bending and stretching of the M–O bonds around the octahedral sites $[T_{2g}(3)]$ and $T_{2g}(2)$, respectively] as well as translation of $T_{2g}(2)$ as well as translation of $T_{2g}(2)$ as well as translation of $T_{2g}(2)$ and $T_{2g}(2)$ as well as translation of $T_{2g}(2)$ the tetrahedral or octahedral sites depend on the mass of the ion occupying the site and the strength of the bonds it forms with the surrounding oxygen atoms. When more than one type of cation occupies the tetrahedral or octahedral sites (i.e., when $T_{2g}(2)$ these modes split into two different peaks corresponding to two different cations, and the relative intensities of these peaks correspond to the inversion parameter.

Figure 5 shows the Raman spectra of 48 nm $\rm ZnFe_2O_4$ and 92 nm $\rm NiFe_2O_4$ nanoparticles. ⁴⁵ Deconvolution of the $\rm NiFe_2O_4$ spectrum demonstrates that each of the five Raman modes can be fitted with two components, indicating at least partial inversion of the spinel structure. ^{46,47} In contrast, the five Raman modes present in the $\rm ZnFe_2O_4$ spectrum each fit to a single peak, which indicates negligible inversion in this material. Indeed, these $\rm NiFe_2O_4$ and $\rm ZnFe_2O_4$ nanocrystals were found to have inversion parameters of $x \sim 0.7$ and 0, respectively. ⁴⁵

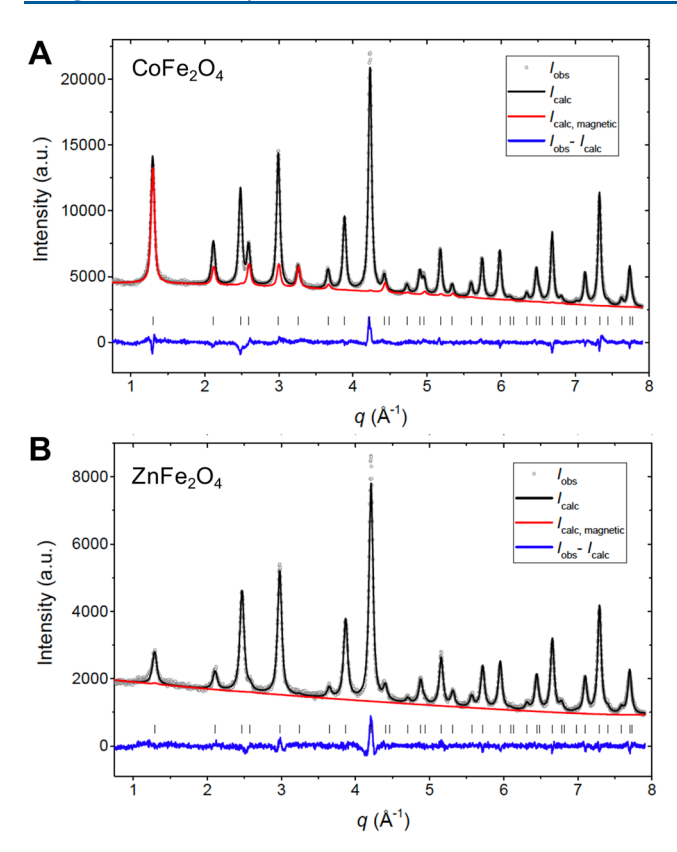


Figure 4. Neutron powder diffraction spectra (open circles) and results of Rietveld refinement (solid black line) obtained for $CoFe_2O_4$ (A) and $ZnFe_2O_4$ (B) nanocrystals. The solid red lines indicate the contribution of magnetic ordering to the neutron powder diffraction pattern. The solid blue lines represent the difference between the observed and calculated spectra. Reproduced with permission from ref 22. Copyright 2018 The Royal Society of Chemistry.

X-ray Photoelectron Spectroscopy (XPS). XPS provides information about the oxidation state, chemical environment, and stoichiometry of the elements present in a material through measurement of the binding energies of their core electrons.4 For spinel ferrite nanoparticles, the 2p region of the metals, particularly iron, can be used to quantify the degree of inversion. This region contains the spin–orbit split $2p_{1/2}$ and $2p_{3/2}$ peaks along with shakeup satellite peaks arising from interactions between the core-hole and any unpaired spins present on the metal center.⁴⁹ cations that occupy the tetrahedral site in a spinel oxide lattice produce 2p peaks with a higher binding energy than the Fe³⁺ ions that occupy octahedral sites. 50–33 Thus, for x > 0, both the $2p_{1/2}$ and $2p_{3/2}$ peaks contain two components whose relative areas are determined by the value of x. For example, Figure 6 shows XPS data collected in the Fe 2p region for ZnFe₂O₄ nanoparticles.⁵³ The 2p_{1/2} and 2p_{3/2} peaks each fit to two components. The higher-energy components at 727.1 eV $(2p_{1/2})$ and 713.0 eV $(2p_{3/2})$, which correspond to Fe³⁺ ions in the tetrahedral sites, each account for 34% of the total area of the $2p_{1/2}$ or $2p_{3/2}$ peak. These data therefore indicate that the magnitude of x is 0.68 for this sample.

X-ray Absorption Spectroscopy. K-edge X-ray absorption nearedge spectroscopy (XANES) and extended X-ray absorption fine structure spectroscopy (EXAFS) provide element-specific information about the oxidation state and coordination number. These techniques are therefore sensitive to the degree of inversion in spinel ferrite nanocrystals. The edge feature in the K-edge XANES spectra of transition metals corresponds to 1s-to-4p transitions, and the position of the edge feature is determined primarily by the oxidation state of the metal. Lower-energy preedge features correspond to 1s-to-3d transitions that are dipole forbidden for metal centers with octahedral

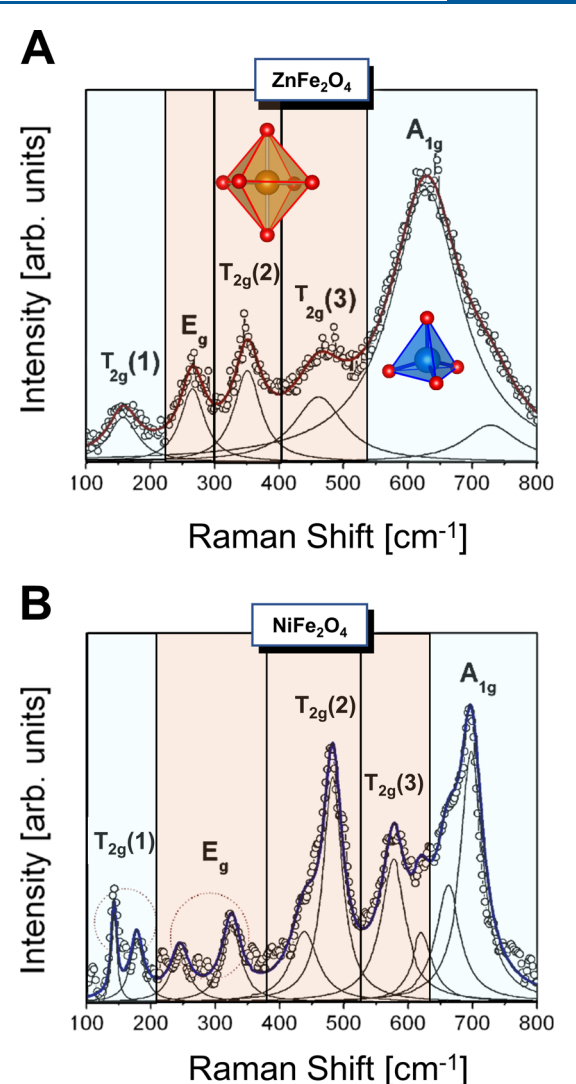


Figure 5. Raman spectra of the (A) NiFe $_2O_4$ (inverse) and (B) ZnFe $_2O_4$ (normal) samples highlighting the impact of inversion on the Raman modes. Orange and blue color-coded rectangles are depicted to associate the modes with the octahedral and tetrahedral site vibrations, respectively. Adapted with permission from ref 45. Copyright 2013 AIP Publishing.

(or centrosymmetric) site symmetry but weakly allowed for metal centers with tetrahedral site symmetry due to the mixing of 3d and 4p orbitals. 54 For spinel ferrites, increased intensity of the preedge peak indicates increased occupancy of the tetrahedral sites by the metal species being examined. In principle, the intensity of the preedge peak relative to the edge peak in Fe or M K-edge XANES spectra can be used to quantify the degree of inversion in MFe $_2$ O $_4$ nanocrystals; however, this approach requires the use of samples with known ratios of tetrahedral and octahedral Fe $^{3+}$ or M^{2+} sites for calibration. 55 Therefore, XANES data are typically used to provide qualitative information about the relative magnitudes of inversion among a set of samples. 21,56,57

In contrast, K-edge EXAFS can be used to quantify the degree of inversion directly. ¹⁷,18,21,55,56,58</sup> EXAFS involves analysis of the interference patterns generated by the scattering of photoelectrons off of atoms adjacent to the absorbing atom. These interference patterns encode the number of atoms with a particular electron density located at various distances from the absorber. ⁵⁹ Structural information from X-ray diffraction data enables prediction of the interference patterns expected for tetrahedral and octahedral sites within the spinel lattice and thereby aids in the accurate fitting of

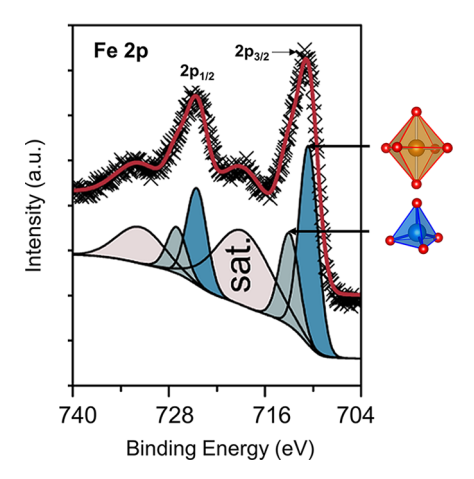


Figure 6. XPS spectra of the Fe 2p core level of as-prepared $\rm ZnFe_2O_4$ nanoparticles. The shaded gray peaks correspond to tetrahedral $\rm Fe^{3^+}$, and the shaded blue peaks correspond to octahedral $\rm Fe^{3^+}$. Adapted with permission from ref 53. Copyright 2016 Beilstein-Institut.

EXAFS data to extract the distribution of metal species among tetrahedral and octahedral sites (i.e., the inversion parameter).¹⁷

X-ray Magnetic Circular Dichroism (XMCD). XMCD spectroscopy employs the differential absorption of left and right circularly polarized X-rays in a magnetic field to provide information about the local electronic and magnetic structures of the absorbing atom. For transition metals, XMCD spectra are usually measured at the L_{2/3} edge, where the 2p core electrons undergo electric-dipole transitions into unoccupied 3d states.⁶⁰ The spectrum is split by the 2p corehole spin-orbit coupling into two main structures: the L_3 and L_2 edges, from the $2p_{3/2} \rightarrow 3d$ and $2p_{1/2} \rightarrow 3d$ transitions, respectively. The spectrum is split by the 2p core-hole spin-orbit coupling into two main structures: the L₃ and L₂ edges, from the $2p_{3/2} \rightarrow 3d$ and $2p_{1/2} \rightarrow 3d$ transitions, respectively. The sign of the XMCD signal depends on the orientation of the magnetic moment of the absorbing atom relative to the external magnetic field. In the spinel ferrite system, because the spins of Fe3+ ions in the tetrahedral sites are coupled antiferromagnetically to those of Fe3+ ions in the octahedral sites, the contribution of tetrahedral Fe³⁺ ions to the XMCD signal has the opposite sign of the contribution of octahedral Fe³⁺ ions. ⁶¹On the basis of the most commonly used sign conventions, the XMCD signal is negative at the L3 edge and positive at the L2 edge for atoms whose magnetic moments are oriented parallel to the external magnetic field.⁶¹ On the basis of the most commonly used sign conventions, the XMCD signal is negative at the L3 edge and positive at the L2 edge for atoms whose magnetic moments are oriented parallel to the external magnetic field. For spinel ferrites, the magnetic moments of the octahedral ions are oriented parallel to the external field. Figure 7 shows an example of Fe L_{2,3}-edge XMCD spectra collected for Fe₃O₄/Mn_xFe_{3-x}O₄ core-shell nanoparticles.⁶² The spectrum has three main peaks at the L3 edge with negative, positive, and then negative intensity as the energy increases. These features are related to the amounts of Fe d⁶ O_h , d⁵ T_{d^4} and d⁵ O_h , respectively, present in the sample. To obtain the relative concentrations of the three different types of iron sites, the experimental spectrum is fitted to a weighted sum of contributions from individual Fe2+ and Fe3+ centers occupying tetrahedral (A) or octahedral (B) sites. The contributions from the individual iron sites are modeled using ligandfield multiplet calculations.⁶² The experimental spectrum contains contributions from Fe3+ ions in both the tetrahedral and octahedral sites and Fe^{2+} ions in the octahedral sites. The absence of a contribution from Fe2+ ions in the tetrahedral sites indicates complete

High-Resolution Scanning Transmission Electron Microscopy (HR-STEM). HR-STEM is an emerging tool for measurement of the local cation distribution in individual spinel oxide nanocrystals with atomic resolution. $^{63-65}$ The sensitivity of the transmitted

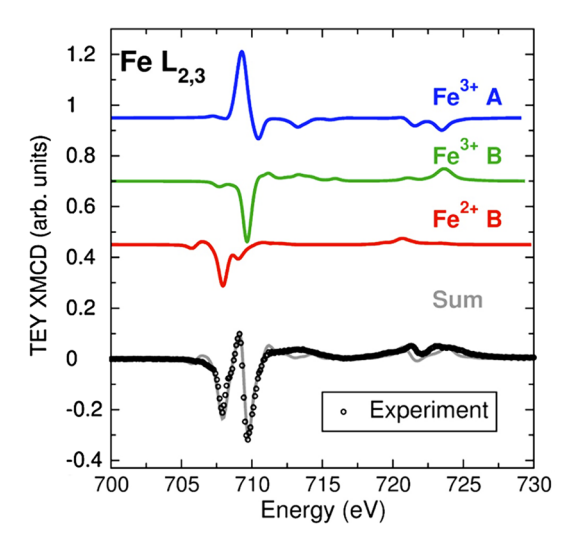


Figure 7. Experimental XMCD spectrum $Fe_3O_4/Mn_xFe_{3-x}O_4$ nanocrystals collected at the Fe $L_{2,3}$ -edge in total electron yield mode at 10 K in an applied field of 1 T (open black circles). The solid gray line plots the fit of these data to a weighted sum of spectra calculated for Fe^{3+} ions in tetrahedral A sites (26% contribution, blue spectrum), Fe^{3+} ions in octahedral B sites (31% contribution, green spectrum), and Fe^{2+} ions in octahedral B sites (43% contribution, red spectrum). Reproduced with permission from ref 62. Copyright 2018 Springer Nature.

electron signal to the atomic number can be used to distinguish between different elements occupying the crystallographic sites observed as "atomic columns" in spinel oxide nanocrystals oriented along particular zone axes.⁶⁴ However, using the transmitted electron signal alone only allows one to make assignments from a set of elements known to be present in the sample based on the relative intensities of the signal (i.e., the heaviest element corresponds to the brightest contrast in a dark-field image).⁶⁴ Coupling HR-STEM to EELS enables absolute identification of various atomic species within the crystallographic sites based on the element-specific locations of the peaks in the energy loss spectra. Analysis of the near-edge structures of the energy loss spectra can even distinguish between the oxidation states of a given element. 63,65 By comparing the known fractions of tetrahedral and octahedral sites present in a particular atomic column with the relative contributions of different elements or oxidation states to the EELS data collected at that column, one can quantify the distribution of elements or oxidation states among the tetrahedral and octahedral sites.

Figure 8 contains STEM-EELS data obtained for Fe₃O₄/Mn₃O₄ core-shell nanocrystals.⁶⁵ Figure 8B shows the STEM high-angle annular dark field (HAADF) image acquired simultaneously with the EELS data for the region highlighted in Figure 8A.⁶⁵ Figure 8B shows the STEM-HAADF image acquired simultaneously with the EELS data for the region highlighted in Figure 8A. This region corresponds to the Fe₃O₄ core of an individual nanocrystal. Figure 8C illustrates the Fe₃O₄ structure along the [541] zone axis, which corresponds to the orientation of the nanocrystal. The red circles indicate octahedral sites, and the blue ovals indicate tetrahedral sites. In Figure 8B, the (111) planes appear as bright columns, which are numbered in the STEM image. These planes contain only octahedral sites, whereas the darker planes between the (111) planes contain both octahedral and tetrahedral sites. Figure 8D shows a 2D plot of the EELS data obtained simultaneously with the image in Figure 8B, where the x axis is the same as that in Figure 8B, the y axis plots the energy loss, and the contrast corresponds to the EELS intensity integrated along the vertical direction in Figure 8B. Figure 8E shows the EELS spectra corresponding to the Fe L3-edge obtained for the bright column labeled 5 in Figure 8B and the dark column immediately to its right (referred to as 5'). Figure 8F plots the onset energy of the Fe L₃-edge

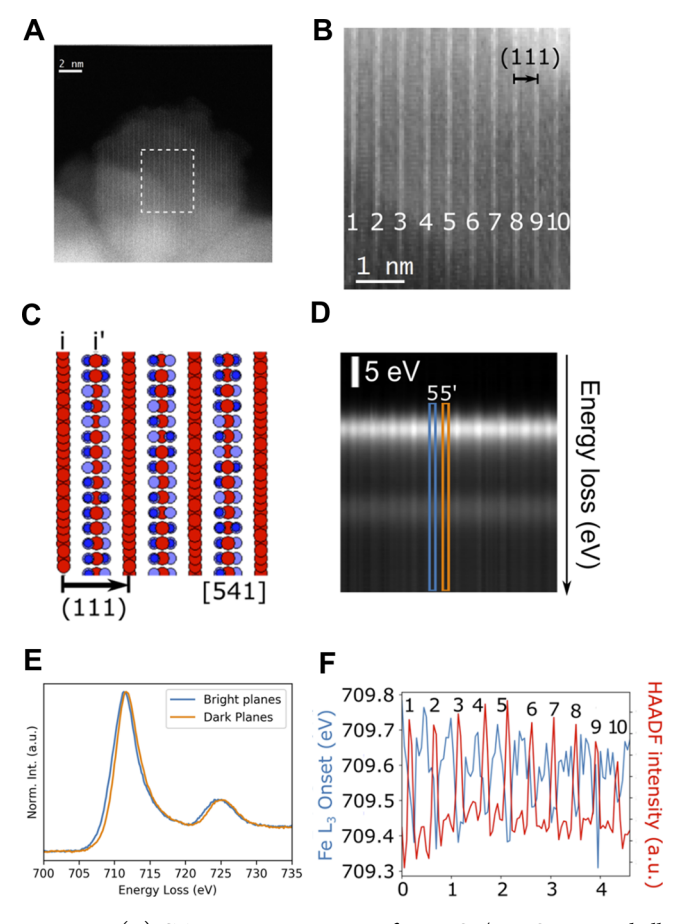


Figure 8. (A) STEM-HAADF image of a Fe₃O₄/Mn₃O₄ core—shell nanocrystal. (B) STEM-HAADF signal coacquired with an EELS spectrum image from the highlighted region in part A corresponding to the Fe₃O₄ core. (C) Illustration of the crystal structure of hematite along the [541] zone axis corresponding to the orientation of the nanocrystal. Red circles depict octahedral sites, purple circles depict tetrahedral sites, and blue circles depict oxygen sites. (D) Plot of the intensity of the Fe L₃-edge EELS signal obtained by integrating along the vertical direction in part B. The horizontal x axis coincides with that from the image shown in part B. (E) EELS spectra collected at positions 5 (blue) and 5′ (orange) corresponding to the highlighted boxes in part D. (F) Plot of the onset energy of the Fe L₃-edge peak and the corresponding HAADF intensity versus horizontal position. Reproduced with permission from ref 65. Copyright 2018 American Chemical Society.

peak and the HAADF intensity versus horizontal position. Altogether, the data in Figure 8 demonstrate that the bright columns exhibit a lower onset energy for the Fe L₃-edge peak than the dark columns. Because the Fe L₃-edge onset shifts to higher energies as the iron oxidation state increases, these data indicate that the bright columns contain a higher ratio of Fe²⁺ to Fe³⁺ than the dark columns, which implies that a larger fraction of Fe²⁺ ions occupy octahedral sites than tetrahedral sites. Indeed, quantitative analysis of these data resulted in a fairly large inversion parameter of $x=0.84\pm0.02$.

All of the characterization methods presented in this section are nondestructive and provide quantitative chemical bonding information that enables determination of the inversion parameter in spinel ferrite nanocrystals. However, they vary in their accessibility and ease of use. The X-ray-based techniques require the use of ultrahigh vacuum systems ($10^{-8}-10^{-11}$ Torr) and, in the case of the X-ray absorption and XMCD techniques, access to a synchrotron source. Neutron powder diffraction also requires specialized facilities with access to a nuclear reactor. Additionally, neutron sources are characterized by relatively low fluxes; therefore, neutron powder

diffraction measurements require large amounts of sample to achieve sufficient signal-to-noise ratios. 66 Mössbauer spectroscopy also requires large amounts of sample or enrichment of the sample with ⁵⁷Fe isotopes in order to achieve sufficient signal-to-noise. ⁶⁶ HR-STEM-EELS measurements provide highly local information with atomic resolution, whereas all of the other techniques described here can only provide data averaged over several particles. Conversely, individual particles characterized by STEM-EELS may not be representative of the entire sample. Of the techniques described here, Raman spectroscopy is generally the most widely available; however. it is also the least direct method for characterizing x and the only one that is not truly element-specific. Finally, all of the techniques described here require deconvolution of multiple contributions to spectral peaks via least-squares fitting procedures of varying complexity that can be prone to significant uncertainties. To minimize the impact of these uncertainties, it is best to use at least two different techniques to quantify x.

IMPACT OF THE CATION DISTRIBUTION ON THE PHYSICAL PROPERTIES OF SPINEL FERRITE NANOCRYSTALS

Electronic Structure. The impact of the inversion parameter on the electronic structure of spinel ferrites has been investigated computationally. These calculations have been used to understand the dependence of other properties, such as conductivity,⁶⁷ magnetism,⁶⁸ and optical absorption, on the cation distribution. The electronic structures of spinel ferrites are calculated using density functional theory (DFT) with the incorporation of a Hubbard correction $(U)^{\frac{1}{10}}$ The local density approximation⁷¹ or generalized gradient approximation⁷² methods alone do not account for the highly localized nature of d orbitals that contribute to the band structure of spinel ferrites, which leads to calculated metallic electronic structures for spinel ferrite materials that are known experimentally to be insulating or semiconducting. 68,70,73,74 To correct for the Coulombic repulsion of the d electrons in spinel ferrites and other transition-metal oxides, U is applied to the transition metal's d orbitals to better represent the local energy cost of electron transfers between neighboring atoms. 70 To determine the appropriate Hubbard correction, chemists apply a range of values until the computed electronic structure matches the experimental data collected for the given system.

As the degree of inversion changes in a spinel ferrite, the number of divalent ions occupying the tetrahedral and octahedral sites changes. The crystal-field splitting for a tetrahedrally coordinated site is smaller than the splitting experienced by the same cation in an octahedral site. Therefore, changing the distribution of M²⁺ and Fe³⁺ cations among the octahedral and tetrahedral sites by changing the degree of inversion will change the energy-level ordering of bands derived from 3d orbitals of the M²⁺ and Fe³⁺ ions, which often leads to a change in the band gap (Table 1). Figure 9

Table 1. Calculated Band Gaps for Normal and Inverted Spinel Ferrites

composition	$E_{\rm g}(x=0)^a$	$E_{\rm g}(x=1)^a$	reference
$MnFe_2O_4$	0.075	0.33	74
Fe_3O_4	0.08	0.72	74
$CoFe_2O_4$	0.22	1.24	72
$NiFe_2O_4$	0.35	1.26	72
CuFe ₂ O ₄	~0	0.603	67
$ZnFe_2O_4$	2.2	2.1	75

^aValues reported as electronvolts.

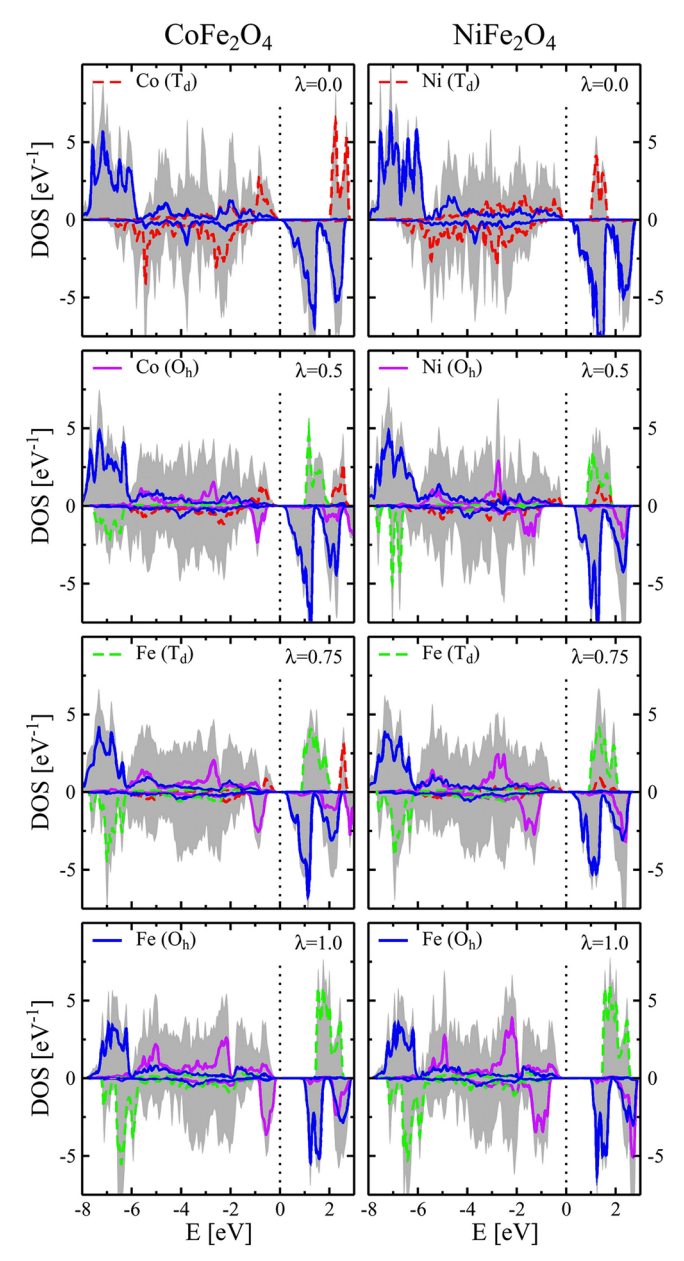


Figure 9. Density of states calculated for $CoFe_2O_4$ (left) and $NiFe_2O_4$ (right) for various values of the inversion parameter λ . The partial density of states associated with tetrahedral cobalt/nickel (red dashed lines), octahedral cobalt/nickel (purple solid lines), tetrahedral iron (dashed green lines), and octahedral iron (solid blue lines) are depicted along with the total density of states (solid gray). Adapted with permission from ref 72. Copyright 2011 AIP Publishing.

shows plots of the orbital contributions to the densities of states obtained for $CoFe_2O_4$ and $NiFe_2O_4$ with various magnitudes of the inversion parameter x. The changes in the energy-level ordering with changes in x observed in these data are representative of those reported for other spinel ferrites where M^{2+} is a paramagnetic 3d ion. 67,68,74 In the normal configuration (x=0), the conduction band minimum comprises octahedral Fe^{3+} orbitals of minority spin polarization. The empty majority spin states derived from the tetrahedral M^{2+} orbitals lie just above these orbitals in energy. The valence band maximum is composed of primarily O 2p character with some contribution from the majority spin states of the tetrahedral M^{2+} ion in the case where M^{2+} contains more

than five 3d electrons. As the degree of inversion increases, the contributions of the M^{2^+} tetrahedral orbitals to the conduction band are replaced by tetrahedral ${\rm Fe}^{3^+}$ orbitals. Additionally, spin minority octahedral orbitals from M^{2^+} contribute to the valence band maximum. The majority spin channel is depicted as positive, and the minority spin channel is depicted as negative. In general, these changes in the energy-level ordering result in an increase in the band gap with increasing inversion, as shown in Table 1, with the exception of ${\rm ZnFe_2O_4},$ for which the degree of inversion has little impact on the calculated band gap. 75

In addition to changing the ordering of various orbital contributions within the conduction and valence bands, changing the degree of inversion also changes the radii of the ions occupying the octahedral and tetrahedral sites. Subsequent rearrangement of the oxygen sublattice in order to accommodate different cation distributions among the octahedral and tetrahedral sites can modify the M–O and Fe–O bond lengths in these sites and thereby modify the electronic structure of the material. For example, as the degree of inversion increases, more M²⁺ ions occupy octahedral sites. Because the M²⁺ ions are larger than the Fe³⁺ ions, the average size of the octahedral sites increases, while that of the tetrahedral sites decreases. The subsequent changes in the M–O bond lengths also contribute to changes in the band structure with inversion.⁷³

Magnetic Properties. The magnetic properties of spinel ferrites are governed by superexchange interactions between the metal cations mediated by the bridging oxygen anions. These superexchange interactions fall into three categories of pairwise interactions: ^{76,77} (i) A-O-B, (ii) B-O-B, and (iii) A-O-A, where A denotes a metal cation in a tetrahedral site and B denotes a metal cation in an octahedral site. The B-O-B and A-O-A interactions occur over bond angles near 90°, whereas the A-O-B interactions occur over bond angles that are more linear (~125°) and therefore allow for more orbital overlap (Figure 10A). According to the Goodenough-Kanamori rules, when the metal cations occupying A and B sites both contribute half-filled orbitals, all three interactions favor antiferromagnetic alignment of the electron spins, with the A-O-B interaction having the exchange coupling constant with the largest magnitude. 76,78,79 However, no spin configuration exists that would accommodate antiferromagnetic alignment of all three types of pairwise interactions simultaneously. Because the A-O-B interaction produces the strongest antiferromagnetic coupling, the lowest-energy spin configuration for metal ferrites containing paramagnetic M²⁺ ions is the one in which all of the B sites are aligned ferromagnetically with respect to each other and antiferromagnetically with respect to the A sites (Figure 10A). ^{76,77} The result is an overall ferrimagnetic alignment with the net magnetization direction aligned with the magnetic moment of the octahedral sites because there are twice as many occupied octahedral sites as tetrahedral sites.

For the normal spinel configuration (x = 0), one expects the saturation magnetization to increase as the magnetic moment of the M^{2+} ions occupying the tetrahedral sites and opposing the magnetic moment of the octahedral Fe^{3+} ions decreases. Thus, because the magnetic moments of the late transition metals decrease in the order $Mn^{2+} > Co^{2+} > Ni^{2+} > Cu^{2+} > Zn^{2+}$, the saturation magnetization of the corresponding spinel ferrite material should increase in the order $MnFe_2O_4 < CoFe_2O_4 < NiFe_2O_4 < CuFe_2O_4 < ZnFe_2O_4$ when $x = 0.^{77}$

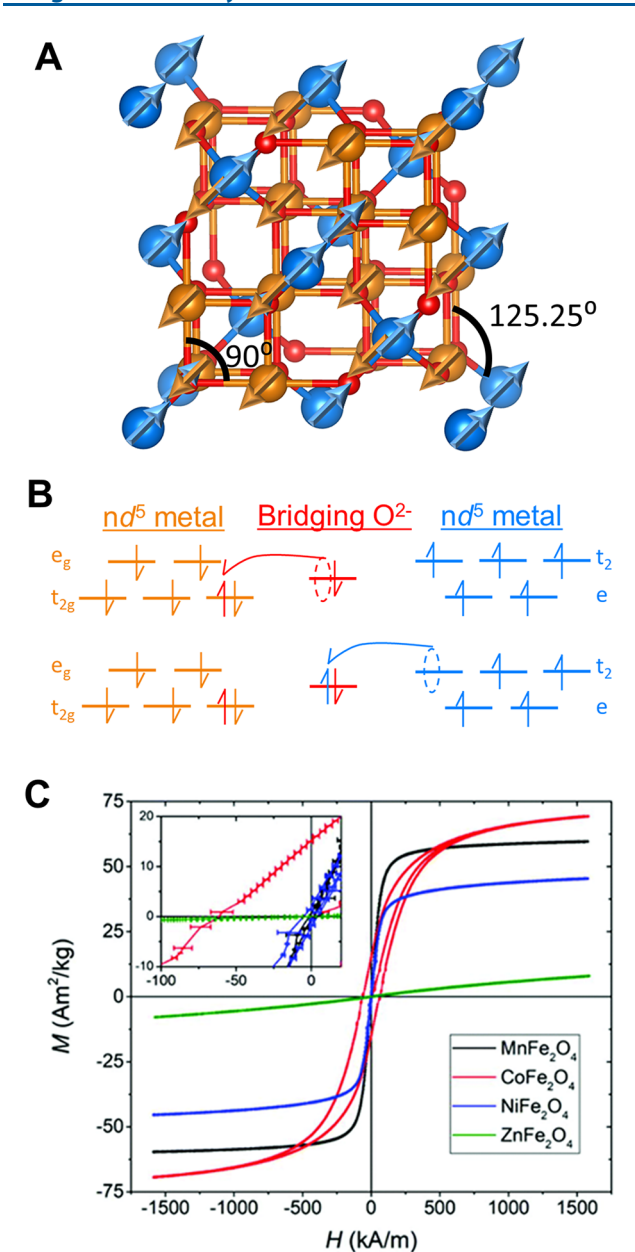


Figure 10. (A) Alignment of the magnetic moments of the tetrahedral atoms (blue) and the antiparallel magnetic moments at the octahedral sites (orange) of MFe $_2$ O $_4$ nanoparticles (M = Mn, Ni, and Zn) with the magnetic moment of the metal centers along the $\langle 111 \rangle$ axis. Adapted with permission from ref 22. Copyright 2018 The Royal Society of Chemistry. (B) Illustration of the superexchange interaction that leads to antiferromagnetic coupling of the octahedral (orange) and tetrahedral (blue) sites. (C) Saturation magnetization curves collected at room temperature for various MFe $_2$ O $_4$ nanoparticles. Reproduced with permission from ref 22. Copyright 2018 The Royal Society of Chemistry.

However, increasing the degree of inversion can disrupt this expected trend. Figure 10C shows magnetization curves for a series of MFe₂O₄ nanocrystals with various degrees of inversion. Within this set of samples, the NiFe₂O₄ nanocrystals have a smaller saturation magnetization than both the CoFe₂O₄ and MnFe₂O₄ nanocrystals, which is the opposite of what is expected for normal spinel ferrites. This discrepancy is explained by the fact that the NiFe₂O₄ sample examined here is completely inverted (x = 1). The exclusive occupancy of the

tetrahedral sites by high-spin Fe³⁺ ions, rather than Ni²⁺ ions, provides a larger magnetic moment opposing that of the octahedral sites, whose average magnetic moment has diminished because of partial occupancy by Ni²⁺. Both effects decrease the magnitude of the saturation magnetization. On the other hand, the CoFe₂O₄ and MnFe₂O₄ samples have similar inversion parameters (x = 0.66 and 0.64, respectively), as measured from neutron diffraction. These inversion parameters correspond to a statistical distribution of M2+ and Fe³⁺ among the (A) and [B] sites. These similar degrees of inversion would be expected to produce a larger saturation magnetization for MnFe₂O₄ compared to CoFe₂O₄; however, the Mn²⁺ ions in MnFe₂O₄ may transfer electrons to Fe³⁺ to form Mn³⁺ and Fe²⁺, thus decreasing the number of unpaired electrons in both cations from five to four, resulting in a decrease in the overall saturation magnetization.^{31,77}

Interestingly, the data in Figure 10C also demonstrate that the ${\rm ZnFe_2O_4}$ nanocrystals exhibit a very minor magnetic response. These nanocrystals have a very small inversion parameter (x=0.17); thus, a majority of the tetrahedral sites are occupied by diamagnetic ${\rm Zn^{2^+}}$ ions. The strong antiferromagnetic exchange interaction between the (A) and [B] sites is therefore no longer operative, and the weak antiferromagnetic coupling of the octahedral sites now dictates the magnetic behavior of the material. 22,77 Consequently, the magnetic ordering temperature in the near-normal ${\rm ZnFe_2O_4}$ is much lower than those of the other spinel ferrites. Increasing the degree of inversion in ${\rm ZnFe_2O_4}$ replaces some of the ${\rm Zn^{2^+}}$ on tetrahedral sites with ${\rm Fe^{3^+}}$ and leads to ferrimagnetic ordering analogous to that observed in metal ferrites where ${\rm M^{2^+}}$ is a paramagnetic ion. 38,81,82

Optical Properties. The assignments of optical transitions observed in spinel ferrite nanocrystals are made based on electronic structure calculations and fall into four main categories, as illustrated in Figure 11:^{57,69,83–85} (i) "ligand-tometal"-type charge-transfer transitions from bands of primarily O 2p character to bands of primarily M or Fe 3d character, (ii) intersublattice charge-transfer transitions between 3d bands arising from Fe³⁺ ions in tetrahedral sites and Fe³⁺ ions in octahedral sites, (iii) intervalent charge-transfer transitions from M²⁺ 3d bands to Fe³⁺ 3d bands, and (iv) crystal-field transitions between 3d bands of M²⁺ or Fe³⁺ cations occupying the same crystallographic site. The crystal-field transitions occur in the near-IR, whereas the charge-transfer-type transitions occur in the visible and ultraviolet regions of the spectrum. Although crystal-field transitions between bands of primarily 3d character are generally forbidden by parity and/or spin selection rules, they may become weakly allowed because of magnetic ordering of neighboring iron centers, distortions of the octahedral site symmetry, or mixing with oxygen orbitals. 85-87 In particular, the intersublattice charge-transfer transitions between 3d orbitals of Fe3+ in tetrahedral sites and 3d orbitals of Fe³⁺ ions in octahedral sites are only allowed if the spins of the two sites adopt an antiparallel alignment, 87 and thus these transitions are only present in spinels where x > 0.

Compared to the magnetic properties, the impact of inversion on the optical properties of spinel ferrite nanocrystals is relatively underexplored. For MFe_2O_4 materials where $M=Zn^{2+}$ or Mg^{2+} , i.e., a diamagnetic cation that does not contain partially filled 3d orbitals, the absorption spectrum is dominated by transitions from O 2p to Fe 3d bands in the visible and ultraviolet regions and crystal-field transitions of the Fe^{3+} ions in the near-IR region. 57,84,85 One study by Granone

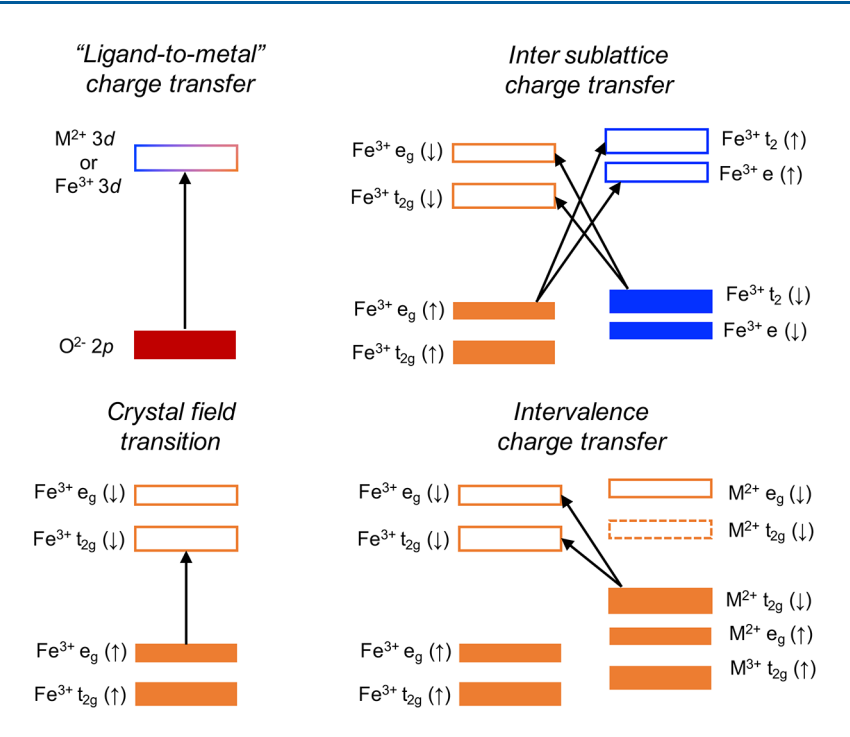


Figure 11. Schematic illustrations of the types of optical transitions found in spinel ferrite nanocrystals. Solid rectangles indicate filled valence bands, and open rectangles indicate empty conduction bands. Orange rectangles indicate bands that arise from metal cations in octahedral sites, and blue rectangles indicate bands that arise from metal cations in tetrahedral sites.

et al. found that the intensity of a transition at 795 nm in $ZnFe_2O_4$ decreases with increasing inversion, whereas another feature centered at 1200 nm broadens as inversion increases (Figure 12). 85 The decrease in intensity of the transition centered at 795 nm was attributed to a loss in intensity of the $^6A_{1g} \rightarrow ^4T_{2g}$ crystal-field transition of octahedral Fe^{3+} ions as the number of Fe^{3+} ions occupying octahedral sites decreases with increasing inversion. The authors attributed the broadening of the peak centered at 1200 nm to increased contributions of crystal-field transitions from Fe^{3+} ions occupying tetrahedral sites upon increased inversion. 85

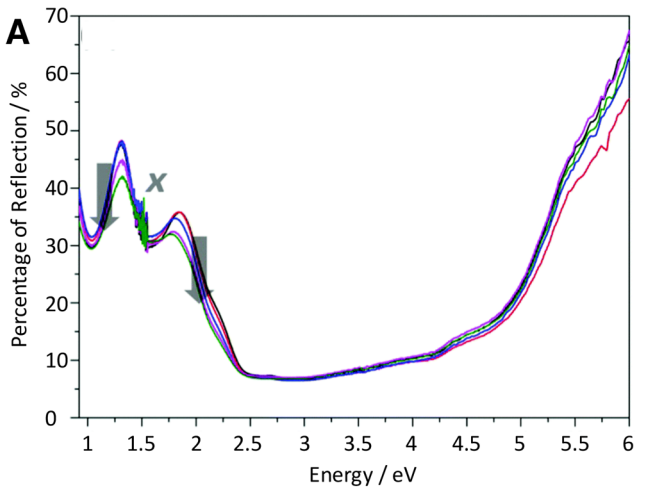
For spinel ferrites where the M^{2+} ion contributes unfilled 3d orbitals to the electronic structure, i.e., $M = Mn^{2+}$, Co^{2+} , Ni^{2+} , and Cu^{2+} , the absorption spectra are dominated by intervalent charge-transfer transitions between 3d bands associated with M^{2+} and Fe^{3+} ions and intersublattice charge-transfer transitions between 3d bands originating from Fe^{3+} ions on tetrahedral and octahedral sites. 69,83,87 Although the dependence of these transitions on the degree of inversion has not been explored in detail, we anticipate that decreasing the degree of inversion will result in a decrease in the intensity of the intersublattice transitions and a shift in the energy of the intervalent charge-transfer transitions as more M^{2+} ions displace Fe^{3+} ions from tetrahedral sites.

SYNTHETIC CONTROL OVER CATION DISTRIBUTION IN SPINEL FERRITE NANOCRYSTALS

The previous sections demonstrate that the electronic, magnetic, and optical properties of spinel ferrites depend on the magnitude of x. Therefore, achieving synthetic control over the cation distribution would enable improved control over these properties. Each spinel ferrite has a thermodynamically preferred degree of inversion determined by its composition.

There are three primarily enthalpic factors that contribute to the thermodynamic stability of a spinel structure with a particular inversion parameter x. 16,19,88 (i) The difference in the ionic radii between the two cations dictates the degree to which the oxygen sublattice must deviate from a cubic closepacked structure to accommodate a particular cation distribution, which is parametrized by the oxygen structure parameter u. This factor generally favors placing the smaller cation in the smaller tetrahedral sites. (ii) Electrostatic stabilization of the primarily ionic spinel oxide lattice favors placing the cation with the larger charge in the octahedral sites, where it is in closer proximity to a larger number of anions to balance its positive charge. However, for certain values of u, where the tetrahedral sites are smaller than the octahedral sites, the smaller distance between the cations and anions in the tetrahedral site results in a larger Coulombic stabilization than that in the octahedral sites even though the total charge is smaller. (iii) Finally, the crystal-field stabilization energy associated with placing a transition-metal ion in a tetrahedral versus octahedral coordination environment also contributes to the relative stability of a particular cation distribution. The entropic contribution to the thermodynamic stability of various cation distributions in spinel ferrites favors a random distribution of cations among the (A) and [B] sites (i.e., x =0.66) but only becomes significant at high temperatures.⁸⁹ For bulk spinel ferrites, heating to high temperatures (>700 K) followed by rapid thermal quenching can "trap" the material in one of these more entropically favored configura-tions. 37,67,85,90,91 Table 2 lists the inversion parameters thermodynamically favored for bulk spinel ferrites at room

For all of these spinel ferrites, Fe^{3+} is smaller than $M^{2+},^{97}$ which means that factor i above favors the inverted structure that places M^{2+} in the larger octahedral sites but factor ii favors the normal structure that places all of the Fe^{3+} ions in the



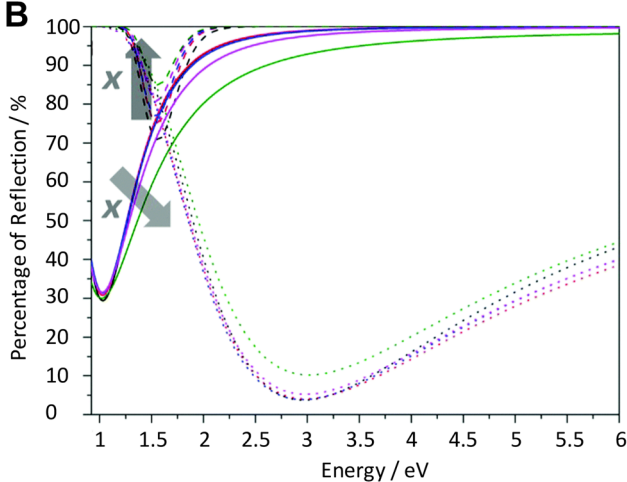


Figure 12. (A) Diffuse-reflectance spectra of $ZnFe_2O_4$ with various degrees of inversion. The gray arrows indicate the evolution in the spectra as x increases from 0.074 to 0.203. (B) Gaussian fits of the three primary absorption features observed as valleys in the diffuse-reflectance spectra at 1.05 eV (solid lines), 1.56 eV (dashed lines), and 3.00 eV (dotted lines). Reproduced with permission from ref 85. Copyright 2018 The Royal Society of Chemistry.

Table 2. Inversion Parameters for Bulk Spinel Ferrites at Room Temperature

composition	bulk value of x	reference
$MgFe_2O_4$	0.90	92
$MnFe_2O_4$	0.20	80, 93
$CoFe_2O_4$	0.93	91
$NiFe_2O_4$	1.0	94
$CuFe_2O_4$	1.0	95
$ZnFe_2O_4$	0	40, 96

octahedral sites for optimal electrostatic stabilization. Indeed, most of the ferrites listed in Table 2 have some degree of inversion. In some cases, crystal-field stabilization energies and other bonding considerations have the deciding influence that determines the final degree of inversion. For example, of the materials included in Table 2, ZnFe_2O_4 is the only ferrite that strongly favors the fully normal spinel configuration (x = 0) in which all of the Zn^{2+} ions occupy tetrahedral sites. In addition to electrostatic effects favoring the normal configuration, the valence 4s and 4p orbitals of Zn^{2+} prefer a tetrahedral bonding

geometry because of their tendency to form strong sp³-type covalent bonds. ^{19,98} In contrast, NiFe₂O₄ prefers to adopt a completely inverse configuration (x=1) in which all of the Ni²+ ions occupy octahedral sites likely because the crystal-field stabilization energies favor an octahedral coordination environment over a tetrahedral coordination environment for the Ni²+ d³ cations.

We note that the thermodynamic considerations described above assume that all coordination sites of the cations in tetrahedral or octahedral configurations are occupied by O²⁻ anions within the lattice. However, cations on the surfaces of spinel ferrite nanocrystals may be coordinatively unsaturated or coordinated to surface ligands. The relative stability of a cation in a particular surface site therefore depends at least in part on its interactions with the surface ligands and/or solvent. The fraction of total cations occupying surface sites depends on the size and shape of the nanocrystal and increases as the size of the nanocrystal decreases. Thus, surface energy considerations may contribute significantly to the thermodynamics governing the cation distribution in small nanocrystals and may help to explain why nanocrystalline spinel ferrites can access a broader range of cation distributions than the corresponding bulk materials. Furthermore, shrinking the size of spinel ferrites from the bulk to the nanoscale provides the opportunity to kinetically trap metastable structural configurations with nonthermodynamic inversion parameters that depend on the synthetic conditions. However, further investigation is needed to understand the relative contributions of the lattice energy, surface energy, and kinetics in determining the cation distributions of spinel ferrite nanocrystals and the roles of various synthetic parameters, such as ligands and solvent, in mediating these contributions.

In this section, we provide an overview of the various methods used to synthesize spinel ferrite nanocrystals and highlight specific cases where tuning the synthetic conditions enabled access to inversion parameters that deviate from those favored by the bulk materials.

General Methods to Access Nanostructured Spinel Metal Ferrites. Methods for synthesizing spinel ferrite nanocrystals include the coprecipitation of metal salts from alkaline aqueous solutions, 26,31 sol-gel methods, 21,55 and thermal decomposition of a mixture of two different metal complexes or one heterobimetallic single-source precursor via (i) heat-up or hot-injection methods at ambient pressure, 18,24,25 (ii) a solvothermal reaction at elevated pressure, 20,80,99 or (iii) microwave-assisted heating. 23,57 Spinel ferrite nanocrystals have also been obtained via mechanochemical processing of bulk materials using methods such as ball-milling in which solid-solid diffusion processes govern the conversion of two binary oxide materials (e.g., ZnO and Fe₂O₃) into one ternary oxide material (e.g., ZnFe₂O₄) and influence the final cation distribution. 38,82 Solid—solid diffusion processes, such as cation hopping, 100 can also drive cation redistribution in hybrid core/shell nanocrystals during the high-temperature solution-phase shell growth reaction. 101 In general, solution-phase synthetic approaches present a major advantage over their solid-state counterparts by providing the opportunity to use surface ligands and precursor solution chemistry to control the size and shape of the nanocrystals while achieving high monodispersity. 102-104

Figure 13 summarizes the types of precursors used in these various synthetic methods. The parameters available to tune these synthetic procedures include the precursor structure,

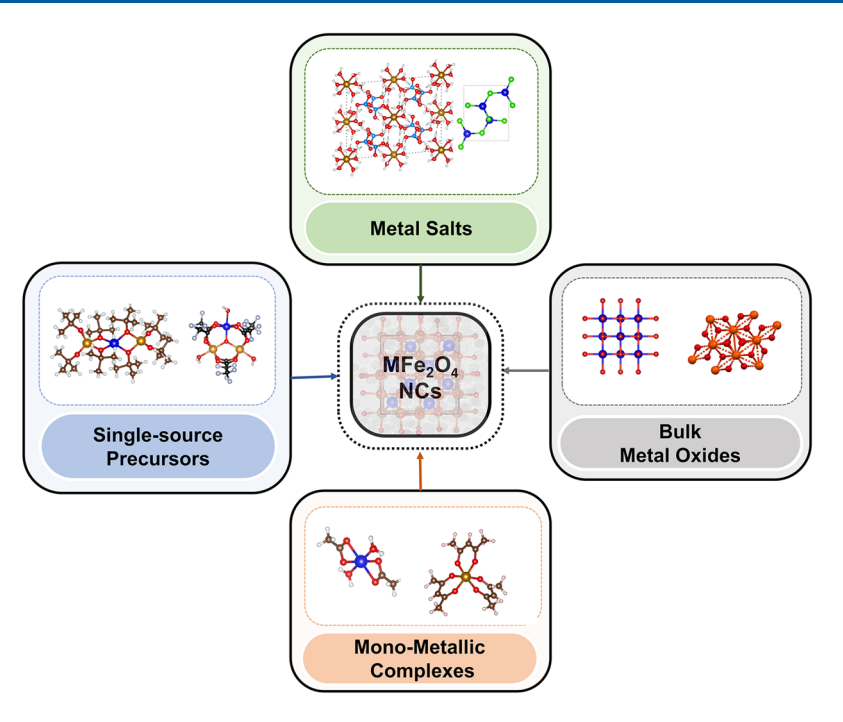


Figure 13. Precursors used in various synthetic methods for making spinel ferrite nanocrystals.

solvent, ligands/surfactant, pH, synthesis temperature and time, and postsynthetic annealing temperature and duration. In addition to tuning the degree of inversion, these synthetic parameters also impact the size, shape, monodispersity, and composition of spinel ferrite nanocrystals. For example, thermal decomposition of heterobimetallic single-source precursors that incorporate both metals in the desired stoichiometry and oxidation state enables access to spinel ferrite nanocrystals with improved monodispersity and phase purity compared to a mixture of homometallic precursors subjected to the same reaction conditions. Methods for synthesizing spinel ferrite nanocrystals are reviewed in detail elsewhere. ^{105,106}

Although a detailed understanding of how to achieve precise synthetic control over the degree of inversion in spinel ferrite nanocrystals is still lacking, here we present a few case studies that provide some indication of strategies that could prove promising. We focus our discussion on NiFe₂O₄ and ZnFe₂O₄, two materials that, in the bulk, are most stable in the completely inverse (x = 1) and normal (x = 0) configurations, respectively (Table 2). The relative strength of the preference of Ni²⁺ for the octahedral sites and Zn²⁺ for the tetrahedral sites is revealed by examining quaternary spinels of composition Ni_{1-y}Zn_yFe₂O₄. Neutron powder diffraction measurements of a series of $Ni_{1-\nu}Zn_{\nu}Fe_{2}O_{4}$ nanocrystals (d =7-27 nm), with y ranging from 0 to 1, found that Ni²⁺ exclusively occupies octahedral sites regardless of the concentration of Zn²⁺, whereas Zn²⁺ occupies both octahedral and tetrahedral sites. 94 The proportion of Zn2+ that occupies tetrahedral sites increases as y increases and with postsynthetic annealing at 600 °C. This study demonstrates that the preference of Ni²⁺ for octahedral sites is stronger than the preference of Zn²⁺ for tetrahedral sites. Therefore, any synthetic method that can access NiFe2O4 nanocrystals with an inversion parameter x < 1 would clearly signal enough kinetic control over the cation distribution to overcome the strong thermodynamic preference of Ni²⁺ for octahedral sites.

One factor that appears to enable access to NiFe2O4 nanocrystals with inversion parameter x < 1 is the presence of a surfactant in the reaction mixture. Tiano et al. synthesized NiFe₂O₄ nanocrystals with diameters of 3.0 nm and x = 0.84via a solvothermal reaction of a basic solution of FeCl₃ and $NiSO_4$ at 220 °C in the presence of the surfactant (aminopropyl)triethoxylsilane (APTES).²⁰ The reaction of the same basic solution of FeCl₃ and NiSO₄ in the absence of APTES produced NiFe₂O₄ nanoparticles with a diameter of 87 nm and x = 1. The decreased inversion parameter obtained in the presence of APTES could be due to the fact that the NiFe₂O₄ nanocrystals synthesized under these conditions are significantly smaller than those obtained in the absence of APTES, although further work is needed to determine whether this is the case. Notably, in the same study, the authors synthesized ZnFe₂O₄ nanocrystals of 3.1 nm diameter with a remarkably high inversion parameter of 0.74 from a solvothermal reaction of ZnCl₂ with APTES.²⁰ Solano et al. made NiFe₂O₄ nanocrystals with a small inversion parameter of x = 0.37 using a heat-up method in which Fe(acac)₃, Ni(acac)2, and the surfactant triethylene glycol were heated to 280 °C for 150 min.²³ The same reaction protocol for $ZnFe_2O_4$ produced nanocrystals with x = 0.36. Importantly, these syntheses do not involve any postsynthetic annealing steps. In contrast, hybrid sol-gel/hydrothermal methods in which metal nitrate precursors are mixed with NaOH or urea to form a gel that is subsequently reacted in an autoclave at elevated temperatures and pressures in the absence of a surfactant form completely inverted NiFe2O4 nanocrystals with $x = 1.^{21,22}$

Another method that enables access to partially inverted NiFe₂O₄ and ZnFe₂O₄ nanocrystals is the use of a heterobimetallic single-source precursor. Abdulwahab et al. synthesized heterobimetallic pivalate complexes Zn₄Fe₂O₂(O₂C(CH₃)₃)₁₀ and NiFe₂O(O₂C(CH₃)₃)₆(HO₂C-(CH₃)₃)₃ and used them as precursors for ZnFe₂O₄ and NiFe₂O₄ nanocrystals, respectively. Injection of the pre-

cursors into a solution of oleylamine, oleic acid, and diphenyl ether at 260 °C produced nanocrystals with the nearly statistically random inversion parameters of 0.66 for ZnFe₂O₄ and 0.69 for NiFe₂O₄. We note that the use of oleic acid in the solvothermal synthesis of CoFe₂O₄ nanocrystals from a mixture of nitrate precursors also produced nanocrystals with diameters that decreased from 19 to 5 nm with increasing oleic acid concentration but statistically random cation inversion parameters ranging from 0.64 to 0.67 that were independent of the particle size. 99

Both surfactants and single-source precursors are known to influence the kinetics of nucleation and growth of metal oxide nanocrystals and thereby impact the size and monodispersity of the resulting nanocrystals. 1,102-104 However, the potential impact of nanocrystal nucleation and growth kinetics on the degree of inversion in spinel ferrite nanocrystals has not been explored in detail to date. On the basis of the results described above, we anticipate that targeted studies of possible links between the kinetics of nucleation and growth and the degree of inversion may provide the key to synthetic control over the cation distribution in spinel ferrite nanocrystals.

■ SUMMARY AND FUTURE OUTLOOK

The electronic, magnetic, and optical properties of spinel ferrite materials of the formula MFe₂O₄ depend on the distribution of M2+ and Fe3+ cations among octahedral and tetrahedral interstitial sites within the cubic close-packed lattice formed by the O2- anions. This cation distribution is quantified by the inversion parameter x, which represents the fraction of M2+ ions that occupy octahedral sites. Characterization techniques that can be used to quantify x include Mössbauer spectroscopy, neutron powder diffraction, Raman spectroscopy, X-ray spectroscopies such as XPS, XMCD, and XANES/EXAFS, and high-resolution STEM coupled to EELS. The impact of the cation distribution on the magnetic properties of spinel ferrite nanocrystals has been investigated extensively, but its impact on the electronic and optical properties of spinel ferrite nanocrystals remains comparatively underexplored. DFT calculations indicate that increasing the magnitude of x results in an increase in the band gap for most bulk spinel ferrites, but this observation has yet to be confirmed experimentally for spinel ferrite nanocrystals. Characterization of the optical absorption spectra of spinel ferrites for various values of x has also been limited to bulk materials of only a few compositions, and the impact of cation distribution on the excited-state dynamics of spinel ferrites has not yet been determined for either bulk or nanocrystalline morphologies.

Compared to bulk materials, nanocrystalline spinel ferrites possess additional structural degrees of freedom that enable access to a broader range of cation distributions. Simultaneous and independent control over the nanoparticle size, shape, composition, and inversion parameter is crucial to enabling investigation of the relationship between the cation distribution and electronic and photophysical properties of spinel ferrite nanocrystals; however, the influence of various synthetic parameters on the degree of inversion remains poorly understood. Developing such knowledge requires carefully designed studies in which synthetic parameters are varied systematically in order to discern their impact on the degree of inversion. Such work would represent a significant contribution to the ability to design versatile spinel ferrite nanocrystals for a

diverse array of applications in magnetic imaging and sensing, information storage, photocatalysis, and energy storage.

AUTHOR INFORMATION

Corresponding Author

Kathryn E. Knowles — Department of Chemistry, University of Rochester, Rochester, New York 14627, United States; orcid.org/0000-0001-6315-6473; Email: kknowles@ur.rochester.edu

Authors

Karla R. Sanchez-Lievanos — Department of Chemistry, University of Rochester, Rochester, New York 14627, United States; orcid.org/0000-0002-6521-7679

James L. Stair — Department of Chemistry, University of Rochester, Rochester, New York 14627, United States; orcid.org/0000-0003-0013-8344

Complete contact information is available at: https://pubs.acs.org/10.1021/acs.inorgchem.1c00040

Author Contributions

The manuscript was written through contributions of all authors.

Notes

The authors declare no competing financial interest.

ACKNOWLEDGMENTS

The authors gratefully acknowledge financial support from the National Science Foundation (grant number CHE 20-44462) and the University of Rochester.

REFERENCES

- (1) Lu, H.; Wright, D. S.; Pike, S. D. The Use of Mixed-metal Single Source Precursors for the Synthesis of Complex Metal Oxides. *Chem. Commun.* **2020**, *56*, 854–871.
- (2) Podjaski, F.; Weber, D.; Zhang, S.; Diehl, L.; Eger, R.; Duppel, V.; Alarcón-Lladó, E.; Richter, G.; Haase, F.; Fontcuberta i Morral, A.; Scheu, C.; Lotsch, B. V. Rational Strain Engineering in Delafossite Oxides for Highly Efficient Hydrogen Evolution Catalysis in Acidic Media. *Nat. Catal.* **2020**, *3*, 55–63.
- (3) Hu, W.; Qin, N.; Wu, G.; Lin, Y.; Li, S.; Bao, D. Opportunity of Spinel Ferrite Materials in Nonvolatile Memory Device Applications Based on Their Resistive Switching Performances. *J. Am. Chem. Soc.* **2012**, *134*, 14658–14661.
- (4) Wang, R.; Wu, J. Structure and Basic Properties of Ternary Metal Oxides and Their Prospects for Application in Supercapacitors. In *Metal Oxides in Supercapacitors*; Dubal, D. P., Gomez-Romero, P., Eds.; Elsevier, 2017; Chapter 5, pp 99–132.
- (5) Redl, F. X.; Cho, K. S.; Murray, C. B.; O'Brien, S. Three-dimensional Binary Superlattices of Magnetic Nanocrystals and Semiconductor Quantum Dots. *Nature* **2003**, *423*, 968–971.
- (6) Abu Ayana, Y. M.; El-Sawy, S. M.; Salah, S. H. Zinc-ferrite Pigment for Corrosion Protection. *Anti-Corros. Methods Mater.* **1997**, 44, 381–388.
- (7) López-Ortega, A.; Lottini, E.; Fernández, C. d. J.; Sangregorio, C. Exploring the Magnetic Properties of Cobalt-Ferrite Nanoparticles for the Development of a Rare-Earth-Free Permanent Magnet. *Chem. Mater.* **2015**, 27, 4048–4056.
- (8) Kumar, Y.; Shirage, P. M. Highest Coercivity and Considerable Saturation Magnetization of CoFe₂O₄ Nanoparticles with Tunable Band Gap Prepared by Thermal Decomposition Approach. *J. Mater. Sci.* **2017**, *52*, 4840–4851.
- (9) Gupta, N. K.; Ghaffari, Y.; Kim, S.; Bae, J.; Kim, K. S.; Saifuddin, M. Photocatalytic Degradation of Organic Pollutants over MFe_2O_4

- (M = Co, Ni, Cu, Zn) Nanoparticles at Neutral pH. Sci. Rep. 2020, 10. 4942.
- (10) Ren, B.; Huang, Y.; Han, C.; Nadagouda, M. N.; Dionysiou, D. D. Ferrites as Photocatalysts for Water Splitting and Degradation of Contaminants. In *Ferrites and Ferrates: Chemistry and Applications in Sustainable Energy and Environmental Remediation*; American Chemical Society, 2016; Vol. 1238; pp 79–112.
- (11) Shinde, P. V.; Shinde, N. M.; Mane, R. S.; Kim, K. H. Ferrites for Electrochemical Supercapacitors. In *Spinel Ferrite Nanostructures for Energy Storage Devices*; Mane, R. S., Jadhav, V. V., Eds.; Elsevier, 2020; Chapter 5, pp 83–122.
- (12) Malaie, K.; Heydari, Z.; Ganjali, M. R. Spinel Nano-ferrites as Low-cost (Photo)electrocatalysts with Unique Electronic Properties in Solar Energy Conversion Systems. *Int. J. Hydrogen Energy* **2021**, *46*, 3510–3529.
- (13) Khalaf, M. M.; Abd El-Lateef, H. M.; Alnajjar, A. O.; Mohamed, I. M. A. A Facile Chemical Synthesis of $Cu_xNi_{(1-x)}Fe_2O_4$ Nanoparticles as a Nonprecious Ferrite Material for Electrocatalytic Oxidation of Acetaldehyde. *Sci. Rep.* **2020**, *10*, 2761.
- (14) Amiri, M.; Salavati-Niasari, M.; Akbari, A. Magnetic Nano-carriers: Evolution of Spinel Ferrites for Medical Applications. *Adv. Colloid Interface Sci.* **2019**, *265*, 29–44.
- (15) Ayesh, A. I.; Abu Haija, M.; Shaheen, A.; Banat, F. Spinel Ferrite Nanoparticles for H₂S Gas Sensor. *Appl. Phys. A: Mater. Sci. Process.* **2017**, *123*, 682.
- (16) Burdett, J. K.; Price, G. D.; Price, S. L. Role of the Crystal-field Theory in Determining the Structures of Spinels. *J. Am. Chem. Soc.* **1982**, *104*, 92–95.
- (17) Henderson, C. M. B.; Charnock, J. M.; Plant, D. A. Cation Occupancies in Mg, Co, Ni, Zn, Al Ferrite Spinels: A Multi-element EXAFS Study. *J. Phys.: Condens. Matter* **2007**, *19*, 076214.
- (18) Ammar, S.; Jouini, N.; Fiévet, F.; Stephan, O.; Marhic, C.; Richard, M.; Villain, F.; Cartier dit Moulin, C.; Brice, S.; Sainctavit, P. Influence of the Synthesis Parameters on the Cationic Distribution of ZnFe₂O₄ Nanoparticles Obtained by Forced Hydrolysis in Polyol Medium. *J. Non-Cryst. Solids* **2004**, *345*–*346*, *658*–*662*.
- (19) O'Neill, H. S. C.; Navrotsky, A. Simple Spinels: Crystallographic Parameters, Cation Radii, Lattice Energies, and Cation Distribution. *Am. Mineral.* **1983**, *68*, 181–194.
- (20) Tiano, A. L.; Papaefthymiou, G. C.; Lewis, C. S.; Han, J.; Zhang, C.; Li, Q.; Shi, C.; Abeykoon, A. M. M.; Billinge, S. J. L.; Stach, E.; Thomas, J.; Guerrero, K.; Munayco, P.; Munayco, J.; Scorzelli, R. B.; Burnham, P.; Viescas, A. J.; Wong, S. S. Correlating Size and Composition-Dependent Effects with Magnetic, Mössbauer, and Pair Distribution Function Measurements in a Family of Catalytically Active Ferrite Nanoparticles. *Chem. Mater.* **2015**, 27, 3572—3592.
- (21) Carta, D.; Casula, M. F.; Falqui, A.; Loche, D.; Mountjoy, G.; Sangregorio, C.; Corrias, A. A Structural and Magnetic Investigation of the Inversion Degree in Ferrite Nanocrystals MFe₂O₄ (M = Mn, Co, Ni). *J. Phys. Chem. C* **2009**, *113*, 8606–8615.
- (22) Andersen, H. L.; Saura-Múzquiz, M.; Granados-Miralles, C.; Canévet, E.; Lock, N.; Christensen, M. Crystalline and Magnetic Structure—property Relationship in Spinel Ferrite Nanoparticles. *Nanoscale* **2018**, *10*, 14902—14914.
- (23) Solano, E.; Frontera, C.; Puig, T.; Obradors, X.; Ricart, S.; Ros, J. Neutron and X-ray Diffraction Study of Ferrite Nanocrystals Obtained by Microwave-assisted Growth. A Structural Comparison with the Thermal Synthetic Route. *J. Appl. Crystallogr.* **2014**, 47, 414–420.
- (24) Abdulwahab, K. O.; Malik, M. A.; O'Brien, P.; Timco, G. A.; Tuna, F.; Muryn, C. A.; Winpenny, R. E. P.; Pattrick, R. A. D.; Coker, V. S.; Arenholz, E. A One-Pot Synthesis of Monodispersed Iron Cobalt Oxide and Iron Manganese Oxide Nanoparticles from Bimetallic Pivalate Clusters. *Chem. Mater.* **2014**, *26*, 999–1013.
- (25) Abdulwahab, K. O.; Malik, M. A.; O'Brien, P.; Timco, G. A.; Tuna, F.; Winpenny, R. E. P.; Pattrick, R. A. D.; Coker, V. S.; Arenholz, E. Hot Injection Thermolysis of Heterometallic Pivalate

- Clusters for the Synthesis of Monodisperse Zinc and Nickel Ferrite Nanoparticles. J. Mater. Chem. C 2014, 2, 6781–6789.
- (26) Kamiyama, T.; Haneda, K.; Sato, T.; Ikeda, S.; Asano, H. Cation Distribution in ZnFe₂O₄ Fine Particles Studied by Neutron Powder Diffraction. *Solid State Commun.* **1992**, *81*, 563–566.
- (27) Vértes, A.; Homonnay, Z. Mössbauer Spectroscopy of Sophisticated Oxides; Akadémiai Kiadó, 1997.
- (28) Perfiliev, Y. D.; Sharma, V. K. Higher Oxidation States of Iron in Solid State: Synthesis and Their Mössbauer Characterization. In *Ferrates*; American Chemical Society, 2008; Vol. 985; pp 112–123.
- (29) Weaver, C. E.; Wampler, J. M.; Pecuil, T. E. Mössbauer Analysis of Iron in Clay Minerals. *Science* 1967, 156, 504–508.
- (30) Fock, J.; Hansen, M. F.; Frandsen, C.; Mørup, S. On the Interpretation of Mössbauer Spectra of Magnetic Nanoparticles. *J. Magn. Magn. Mater.* **2018**, *445*, 11–21.
- (31) Zhang, Z. J.; Wang, Z. L.; Chakoumakos, B. C.; Yin, J. S. Temperature Dependence of Cation Distribution and Oxidation State in Magnetic Mn–Fe Ferrite Nanocrystals. *J. Am. Chem. Soc.* **1998**, 120, 1800–1804.
- (32) Greenwood, N. N.; Gibb, T. C. Mössbauer Spectroscopy; Chapman and Hall: London, 1971.
- (33) Roumaih, K.; Manapov, R. A.; Sadykov, E. K.; Pyataev, A. V. Mössbauer Studies of $Cu_{1-x}Ni_x$ FeMnO₄ Spinel Ferrites. *J. Magn. Magn. Mater.* **2005**, 288, 267–275.
- (34) Watson, R. E.; Freeman, A. J. Origin of Effective Fields in Magnetic Materials. *Phys. Rev.* **1961**, *123*, 2027–2047.
- (35) Rao, K. H.; Raju, S. B.; Mendiratta, R. G.; Eymery, J. P. Hyperfine Fields in Cr and In Substituted Mn—Zn Ferrites. *Solid State Commun.* **1983**, *45*, 919–923.
- (36) Kurian, J.; John, S. P.; Jacob, M. M.; Reddy, V. R.; Abraham, K. E.; Prasad, V. S. Mössbauer Studies of Nanocrystalline ZnFe₂O₄ Particles Prepared by Spray Pyrolysis Method. *IOP Conf. Ser.: Mater. Sci. Eng.* **2015**, *73*, 012032.
- (37) O'Neill, H. S. C.; Annersten, H.; Virgo, D. The Temperature Dependence of the Cation Distribution in Magnesioferrite (MgFe₂O₄) from Powder XRD Structural Refinements and Mössbauer Spectroscopy. *Am. Mineral.* **1992**, *77*, 725–740.
- (38) Šepelák, V.; Tkáčová, K.; Boldyrev, V. V.; Wiβmann, S.; Becker, K. D. Mechanically Induced Cation Redistribution in ZnFe₂O₄ and its Thermal Stability. *Phys. B* **1997**, 234–236, 617–619.
- (39) Copley, J. R. D. The Fundamentals of Neutron Powder Diffraction; National Institute of Standards and Technology: Washington, DC, 2001.
- (40) Bræstrup, F.; Hauback, B. C.; Hansen, K. K. Temperature Dependence of the Cation Distribution in ZnFe₂O₄ Measured with High Temperature Neutron Diffraction. *J. Solid State Chem.* **2008**, 181, 2364–2369.
- (41) Massoudi, J.; Smari, M.; Nouri, K.; Dhahri, E.; Khirouni, K.; Bertaina, S.; Bessais, L.; Hlil, E. K. Magnetic and Spectroscopic Properties of Ni–Zn–Al Ferrite Spinel: From the Nanoscale to Microscale. *RSC Adv.* **2020**, *10*, 34556–34580.
- (42) Jacintho, G. V. M.; Brolo, A. G.; Corio, P.; Suarez, P. A. Z.; Rubim, J. C. Structural Investigation of MFe_2O_4 (M = Fe, Co) Magnetic Fluids. *J. Phys. Chem. C* **2009**, *113*, 7684–7691.
- (43) Wang, W.; Ding, Z.; Zhao, X.; Wu, S.; Li, F.; Yue, M.; Liu, J. P. Microstructure and Magnetic Properties of MFe_2O_4 (M=Co, Ni, and Mn) Ferrite Nanocrystals Prepared Using Colloid Mill and Hydrothermal Method. *J. Appl. Phys.* **2015**, *117*, 17A328.
- (44) Iliev, M. N.; Mazumdar, D.; Ma, J. X.; Gupta, A.; Rigato, F.; Fontcuberta, J. Monitoring *B*-site Ordering and Strain Relaxation in NiFe₂O₄ Epitaxial Films by Polarized Raman Spectroscopy. *Phys. Rev. B: Condens. Matter Mater. Phys.* **2011**, 83, 014108.
- (45) Lazarević, Z. Ž.; Jovalekić, Č.; Milutinović, A.; Sekulić, D.; Ivanovski, V. N.; Rečnik, A.; Cekić, B.; Romčević, N. Ž. Nanodimensional Spinel NiFe₂O₄ and ZnFe₂O₄ Ferrites Prepared by Soft Mechanochemical Synthesis. *J. Appl. Phys.* **2013**, *113*, 187221.
- (46) Ahlawat, A.; Sathe, V. G. Raman study of NiFe2O4 nanoparticles, bulk and films: effect of laser power. *J. Raman Spectrosc.* **2011**, 42, 1087–1094.

- (47) Sousa, M. H.; Tourinho, F. A.; Rubim, J. C. Use of Raman Micro-spectroscopy in The Characterization of $M^{II}Fe_2O_4$ (M = Fe, Zn) Electric Double Layer Ferrofluids. *J. Raman Spectrosc.* **2000**, *31*, 185–191.
- (48) Engelhard, M. H.; Droubay, T. C.; Du, Y. X-Ray Photoelectron Spectroscopy Applications. In *Encyclopedia of Spectroscopy and Spectrometry*, 3rd ed.; Lindon, J. C., Tranter, G. E., Koppenaal, D. W., Eds.; Academic Press: Oxford, U.K., 2017; pp 716–724.
- (49) Tougaard, S. Surface Analysis: X-ray Photoelectron Spectroscopy. In *Encyclopedia of Analytical Science*; 3rd ed.; Worsfold, P., Poole, C., Townshend, A., Miró, M., Eds.; Academic Press: Oxford, U.K., 2013; pp 400–409.
- (50) Zhou, Z.; Zhang, Y.; Wang, Z.; Wei, W.; Tang, W.; Shi, J.; Xiong, R. Electronic Structure Studies of the Spinel CoFe₂O₄ by X-ray Photoelectron Spectroscopy. *Appl. Surf. Sci.* **2008**, 254, 6972–6975.
- (51) Gu, Z.; Xiang, X.; Fan, G.; Li, F. Facile Synthesis and Characterization of Cobalt Ferrite Nanocrystals via a Simple Reduction—Oxidation Route. *J. Phys. Chem. C* **2008**, *112*, 18459—18466
- (52) Reitz, C.; Suchomski, C.; Haetge, J.; Leichtweiss, T.; Jagličić, Z.; Djerdj, I.; Brezesinski, T. Soft-templating Synthesis of Mesoporous Magnetic CuFe₂O₄ Thin Films with Ordered 3D Honeycomb Structure and Partially Inverted Nanocrystalline Spinel Domains. *Chem. Commun.* **2012**, 48, 4471–4473.
- (53) Suchomski, C.; Breitung, B.; Witte, R.; Knapp, M.; Bauer, S.; Baumbach, T.; Reitz, C.; Brezesinski, T. Microwave Synthesis of High-quality and Uniform 4 nm ZnFe₂O₄ Nanocrystals for Application in Energy Storage and Nanomagnetics. *Beilstein J. Nanotechnol.* **2016**, *7*, 1350–1360.
- (54) Grunes, L. A. Study of the K edges of 3d Transition Metals in Pure and Oxide form by X-ray-absorption Spectroscopy. *Phys. Rev. B: Condens. Matter Mater. Phys.* **1983**, 27, 2111–2131.
- (55) Akhtar, M. J.; Nadeem, M.; Javaid, S.; Atif, M. Cation Distribution in Nanocrystalline ZnFe₂O₄ Investigated Using X-ray Absorption Fine Structure Spectroscopy. *J. Phys.: Condens. Matter* **2009**, *21*, 405303.
- (56) Carta, D.; Marras, C.; Loche, D.; Mountjoy, G.; Ahmed, S. I.; Corrias, A. An X-ray Absorption Spectroscopy Study of the Inversion Degree in Zinc Ferrite Nanocrystals Dispersed on a Highly Porous Silica Aerogel Matrix. *J. Chem. Phys.* **2013**, *138*, 054702.
- (57) Bloesser, A.; Kurz, H.; Timm, J.; Wittkamp, F.; Simon, C.; Hayama, S.; Weber, B.; Apfel, U.-P.; Marschall, R. Tailoring the Size, Inversion Parameter, and Absorption of Phase-Pure Magnetic MgFe₂O₄ Nanoparticles for Photocatalytic Degradations. *ACS Appl. Nano Mater.* **2020**, *3*, 11587–11599.
- (58) Carta, D.; Casula, M. F.; Mountjoy, G.; Corrias, A. Formation and Cation Distribution in Supported Manganese Ferrite Nanoparticles: An X-ray Absorption Study. *Phys. Chem. Chem. Phys.* **2008**, *10*, 3108–3117.
- (59) Agarwal, B. K. X-ray Spectroscopy: An Introduction, 2nd ed.; Springer-Verlag: Heidelberg, Germany, 1991.
- (60) Van Der Laan, G.; Thole, B. T. Strong Magnetic X-ray Dichroism in 2p Absorption Spectra of 3d Transition-metal Ions. Phys. Rev. B: Condens. Matter Mater. Phys. 1991, 43, 13401–13411.
- (61) Stöhr, J.; Wu, Y. X-Ray Magnetic Circular Dichroism: Basic Concepts and Theory for 3D Transition Metal Atoms. In *New Directions in Research with Third-Generation Soft X-Ray Synchrotron Radiation Sources*; NATO ASI Series (Series E: Applied Sciences); Schlachter, A. S., Wuilleumier, F. J., Eds.; Springer: Dordrecht, 1994; Vol. 254; pp 221-250.
- (62) Oberdick, S. D.; Abdelgawad, A.; Moya, C.; Mesbahi-Vasey, S.; Kepaptsoglou, D.; Lazarov, V. K.; Evans, R. F. L.; Meilak, D.; Skoropata, E.; van Lierop, J.; Hunt-Isaak, I.; Pan, H.; Ijiri, Y.; Krycka, K. L.; Borchers, J. A.; Majetich, S. A. Spin Canting Across Core/shell Fe₃O₄/Mn_xFe_{3-x}O₄ Nanoparticles. *Sci. Rep.* **2018**, *8*, 3425.
- (63) Tan, H.; Turner, S.; Yücelen, E.; Verbeeck, J.; Van Tendeloo, G. 2D Atomic Mapping of Oxidation States in Transition Metal Oxides by Scanning Transmission Electron Microscopy and Electron Energy-Loss Spectroscopy. *Phys. Rev. Lett.* **2011**, *107*, 107602.

- (64) Bao, L.; Zang, J.; Wang, G.; Li, X. Atomic-Scale Imaging of Cation Ordering in Inverse Spinel Zn₂SnO₄ Nanowires. *Nano Lett.* **2014**, *14*, 6505–6509.
- (65) Torruella, P.; Ruiz-Caridad, A.; Walls, M.; Roca, A. G.; López-Ortega, A.; Blanco-Portals, J.; López-Conesa, L.; Nogués, J.; Peiró, F.; Estradé, S. Atomic-Scale Determination of Cation Inversion in Spinel-Based Oxide Nanoparticles. *Nano Lett.* **2018**, *18*, 5854–5861.
- (66) Blakeley, M. P.; Langan, P.; Niimura, N.; Podjarny, A. Neutron Crystallography: Opportunities, Challenges, and Limitations. *Curr. Opin. Struct. Biol.* **2008**, *18*, 593–600.
- (67) Zhang, R.; Yuan, Q.; Ma, R.; Liu, X.; Gao, C.; Liu, M.; Jia, C.-L.; Wang, H. Tuning Conductivity and Magnetism of CuFe₂O₄ via Cation Redistribution. *RSC Adv.* **2017**, *7*, 21926–21932.
- (68) Hou, Y. H.; Zhao, Y. J.; Liu, Z. W.; Yu, H. Y.; Zhong, X. C.; Qiu, W. Q.; Zeng, D. C.; Wen, L. S. Structural, Electronic and Magnetic Properties of Partially Inverse Spinel CoFe₂O₄: A First-principles Study. *J. Phys. D: Appl. Phys.* **2010**, *43*, 445003.
- (69) Fontijn, W. F. J.; van der Zaag, P. J.; Feiner, L. F.; Metselaar, R.; Devillers, M. A. C. A Consistent Interpretation of the Magneto-optical Spectra of Spinel Type Ferrites (invited). *J. Appl. Phys.* **1999**, *85*, 5100–5105.
- (70) Anisimov, V. I.; Zaanen, J.; Andersen, O. K. Band Theory and Mott Insulators: Hubbard U Instead of Stoner I. *Phys. Rev. B: Condens. Matter Mater. Phys.* **1991**, *44*, 943–954.
- (71) Anisimov, V. I.; Aryasetiawan, F.; Lichtenstein, A. I. First-principles Calculations of the Electronic Structure and Spectra of Strongly Correlated Systems: The LDA+U Method. *J. Phys.: Condens. Matter* **1997**, *9*, 767–808.
- (72) Fritsch, D.; Ederer, C. Effect of epitaxial strain on the cation distribution in spinel ferrites CoFe₂O₄ and NiFe₂O₄: A density functional theory study. *Appl. Phys. Lett.* **2011**, *99*, 081916.
- (73) Soliman, S.; Elfalaky, A.; Fecher, G. H.; Felser, C. Electronic Structure Calculations for ZnFe₂O₄. *Phys. Rev. B: Condens. Matter Mater. Phys.* **2011**, 83, 085205.
- (74) Szotek, Z.; Temmerman, W. M.; Ködderitzsch, D.; Svane, A.; Petit, L.; Winter, H. Electronic Structures of Normal and Inverse Spinel Ferrites from First Principles. *Phys. Rev. B: Condens. Matter Mater. Phys.* **2006**, *74*, 174431.
- (75) Melo Quintero, J. J.; Salcedo Rodríguez, K. L.; Rodríguez Torres, C. E.; Errico, L. A. Ab Initio Study of the Role of Defects on the Magnetic Response and the Structural, Electronic and Hyperfine Properties of $ZnFe_2O_4$. J. Alloys Compd. **2019**, 775, 1117–1128.
- (76) Srivastava, C. M.; Srinivasan, G.; Nanadikar, N. G. Exchange Constants in Spinel Ferrites. *Phys. Rev. B: Condens. Matter Mater. Phys.* **1979**, *19*, 499–508.
- (77) Chikazumi, S.; Graham, C. D. Physics of Ferromagnetism; Oxford University Press: Oxford, U.K., 1997.
- (78) Goodenough, J. B. Theory of the Role of Covalence in the Perovskite-Type Manganites [La,M(II)]MnO₃. *Phys. Rev.* **1955**, *100*, 564–573.
- (79) Kanamori, J. Superexchange Interaction and Symmetry Properties of Electron Orbitals. J. Phys. Chem. Solids 1959, 10, 87–98.
- (80) Vamvakidis, K.; Katsikini, M.; Sakellari, D.; Paloura, E. C.; Kalogirou, O.; Dendrinou-Samara, C. Reducing the Inversion Degree of MnFe₂O₄ Nanoparticles through Synthesis to Enhance Magnetization: Evaluation of Their ¹H NMR Relaxation and Heating Efficiency. *Dalton Trans.* **2014**, *43*, 12754–12765.
- (81) Mozaffari, M.; Eghbali Arani, M.; Amighian, J. The Effect of Cation Distribution on Magnetization of ZnFe₂O₄ Nanoparticles. *J. Magn. Magn. Mater.* **2010**, 322, 3240–3244.
- (82) Harris, V. G.; Šepelák, V. Mechanochemically Processed Zinc Ferrite Nanoparticles: Evolution of Structure and Impact of Induced Cation Inversion. *J. Magn. Magn. Mater.* **2018**, *465*, 603–610.
- (83) Kim, K. J.; Lee, H. S.; Lee, M. H.; Lee, S. H. Comparative Magneto-optical Investigation of d-d Charge—transfer Transitions in Fe₃O₄, CoFe₂O₄, and NiFe₂O₄. *J. Appl. Phys.* **2002**, *91*, 9974—9977.
- (84) Pailhé, N.; Wattiaux, A.; Gaudon, M.; Demourgues, A. Correlation between Structural Features and Vis–NIR Spectra of α -

- Fe_2O_3 Hematite and AFe_2O_4 Spinel Oxides (A = Mg, Zn). J. Solid State Chem. **2008**, 181, 1040–1047.
- (85) Granone, L. I.; Ulpe, A. C.; Robben, L.; Klimke, S.; Jahns, M.; Renz, F.; Gesing, T. M.; Bredow, T.; Dillert, R.; Bahnemann, D. W. Effect of the Degree of Inversion on Optical Properties of Spinel ZnFe₂O₄. *Phys. Chem. Chem. Phys.* **2018**, 20, 28267–28278.
- (86) Himcinschi, C.; Vrejoiu, I.; Salvan, G.; Fronk, M.; Talkenberger, A.; Zahn, D. R. T.; Rafaja, D.; Kortus, J. Optical and magneto-optical study of nickel and cobalt ferrite epitaxial thin films and submicron structures. *J. Appl. Phys.* **2013**, *113*, 084101.
- (87) Zviagin, V.; Richter, P.; Böntgen, T.; Lorenz, M.; Ziese, M.; Zahn, D. R. T.; Salvan, G.; Grundmann, M.; Schmidt-Grund, R. Comparative study of optical and magneto-optical properties of normal, disordered, and inverse spinel-type oxides. *Phys. Status Solidi B* **2016**, 253, 429–436.
- (88) Valenzuela, R. Novel Applications of Ferrites. *Phys. Res. Int.* **2012**, 2012, 591839.
- (89) Veverka, M.; Jirák, Z.; Kaman, O.; Knížek, K.; Maryško, M.; Pollert, E.; Závěta, K.; Lančok, A.; Dlouhá, M.; Vratislav, S. Distribution of Cations in Nanosize and Bulk Co–Zn Ferrites. *Nanotechnology* **2011**, 22, 345701.
- (90) Chandramohan, P.; Srinivasan, M. P.; Velmurugan, S.; Narasimhan, S. V. Cation Distribution and Particle Size Effect on Raman Spectrum of CoFe₂O₄. *J. Solid State Chem.* **2011**, *184*, 89–96.
- (91) Sawatzky, G. A.; Van Der Woude, F.; Morrish, A. H. Mössbauer Study of Several Ferrimagnetic Spinels. *Phys. Rev.* **1969**, 187, 747–757.
- (92) Franco, A., Jr.; Silva, M. S. High Temperature Magnetic Properties of Magnesium Ferrite Nanoparticles. *J. Appl. Phys.* **2011**, *109*, 07B505.
- (93) Grimes, R. W.; Anderson, A. B.; Heuer, A. H. Predictions of Cation Distributions in AB_2O_4 Spinels from Normalized Ion Energies. *J. Am. Chem. Soc.* **1989**, *111*, 1–7.
- (94) Hölscher, J.; Andersen, H. L.; Saura-Múzquiz, M.; Garbus, P. G.; Christensen, M. Correlation Between Microstructure, Cation Distribution and Magnetism in Ni_{1-x}Zn_xFe₂O₄ Nanocrystallites. *CrystEngComm* **2020**, 22, 515–524.
- (95) Balagurov, A. M.; Bobrikov, I. A.; Maschenko, M. S.; Sangaa, D.; Simkin, V. G. Structural Phase Transition in CuFe₂O₄ Spinel. *Crystallogr. Rep.* **2013**, *58*, 710–717.
- (96) O'Neill, H. S. C. Temperature Dependence of the Cation Distribution in Zinc Ferrite (ZnFe₂O₄) from Powder XRD Structural Refinements. *Eur. J. Mineral.* **1992**, *4*, 571–580.
- (97) Shannon, R. D. Revised Effective Ionic Radii and Systematic Studies of Interatomic Distances in Halides and Chalcogenides. *Acta Crystallogr., Sect. A: Cryst. Phys., Diffr., Theor. Gen. Crystallogr.* 1976, 32, 751–767.
- (98) Verwey, E. J. W.; Heilmann, E. L. Physical Properties and Cation Arrangement of Oxides with Spinel Structures I. Cation Arrangement in Spinels. *J. Chem. Phys.* **1947**, *15*, 174–180.
- (99) Jovanović, S.; Spreitzer, M.; Tramšek, M.; Trontelj, Z.; Suvorov, D. Effect of Oleic Acid Concentration on the Physicochemical Properties of Cobalt Ferrite Nanoparticles. *J. Phys. Chem. C* **2014**, *118*, 13844–13856.
- (100) Muhich, C. L.; Aston, V. J.; Trottier, R. M.; Weimer, A. W.; Musgrave, C. B. First-Principles Analysis of Cation Diffusion in Mixed Metal Ferrite Spinels. *Chem. Mater.* **2016**, *28*, 214–226.
- (101) Rivas-Murias, B.; Testa-Anta, M.; Torruella, P.; Estradé, S.; Peiró, F.; Rodríguez-González, B.; Comesaña-Hermo, M.; Salgueiriño, V. Structural and Magnetic Implications of Transition Metal Migration within Octahedral Core—Shell Nanocrystals. *Chem. Mater.* **2020**, *32*, 10435—10446.
- (102) Qiao, L.; Swihart, M. T. Solution-Phase Synthesis of Transition Metal Oxide Nanocrystals: Morphologies, Formulae, and Mechanisms. *Adv. Colloid Interface Sci.* **2017**, 244, 199–266.
- (103) Brewster, D. A.; Sarappa, D. J.; Knowles, K. E. Role of Aliphatic Ligands and Solvent Composition in the Solvothermal Synthesis of Iron Oxide Nanocrystals. *Polyhedron* **2019**, *157*, 54–62.

- (104) Sanchez-Lievanos, K. R.; Tariq, M.; Brennessel, W. W.; Knowles, K. E. Heterometallic Trinuclear Oxo-centered Clusters as Single-source Precursors for Synthesis of Stoichiometric Monodisperse Transition Metal Ferrite Nanocrystals. *Dalton Trans.* **2020**, 49, 16348–16358.
- (105) Kumar, M.; Singh Dosanjh, H.; Sonika; Singh, J.; Monir, K.; Singh, H. Review on Magnetic Nanoferrites and Their Composites as Alternatives in Waste Water Treatment: Synthesis, Modifications and Applications. *Environ. Sci. Water Res. Technol.* **2020**, *6*, 491–514.
- (106) Galvao, W. S.; Neto, D. M. A.; Freire, R. M.; Fechine, P. B. A. Super-Paramagnetic Nanoparticles with Spinel Structure: A Review of Synthesis and Biomedical Applications. *Solid State Phenom.* **2015**, 241, 139–176.